

Thin Disc Flight Dynamics with Applications to Ballochore Seed Dispersal

Thesis by
Joe Hesse-Withbroe

In Partial Fulfillment of the Requirements for the
Degree of
Bachelor of Arts, Physics



POMONA COLLEGE
Claremont, California

December 2021
Defended December 2021

© December 2021

Joe Hesse-Withbroe
ORCID: 0000-0001-6812-5369

All rights reserved

ACKNOWLEDGEMENTS

The creation of this thesis would not have been possible without significant support from a number of people. First, I thank Eric Cooper and all those who supported him in his initial analyses of *Ruellia ciliatiflora* flight dynamics. This thesis is a direct extension of Eric's work and would not be nearly as detailed were it not for Eric's extensive foundational work. Thank you to Eric and all those who supported him for creating a solid foundation that launched my own work.

Second, I thank my advisor Professor Whitaker for his continual support over this year. His insight and advice has been invaluable throughout the creation of this thesis, helping to resolve outstanding issues and fact check my results. Thank you for your support and for giving this physicist a little bit of appreciation for the "soft science" of biology.

Third, I thank my fellow denizens of Estella Laboratory, without whom I would certainly not have made it to the other side with a physics degree. I thank the physics class of '21 who created a warm and welcoming community for our entering class, and my current and former class of '22 for their support and kindness over these last four years. While we're now displaced over 3+ graduating semesters, I'll never forget the late nights spent together in Estella in our first years.

Fourth, I thank my family for their unconditional support in all of my endeavors. Despite being the only science-minded individual in the immediate family, I thank you for at minimum feigning interest in my research and supporting me in whatever I choose to do.

Finally, I thank the cross country team and its adjacent supporters. The kindness shown to me by the team in my first year assured me I made the right decision in coming to Pomona. The grit, passion, and determination you show every day is beyond inspirational, and the strength of the community and culture you all have helped to create is unparalleled. The privilege of running with you over these last four years has, without a doubt, been the highlight of time at Pomona. I am beyond proud of the team I am leaving behind, and look forward to following along with your future successes. PAY KYLE.

ABSTRACT

In this thesis, an equation of motion for a thin, spinning disc moving in a fluid medium is developed and used to examine seed dispersal biology. It is shown that backspin is the only stable disc orientation, while topspin is metastable. The backspin orientation is the minimal drag orientation, but is not necessarily the range maximizing orientation, as non-backspin orientations experience a lifting force that can keep the disc aloft far longer than in the backspin case. The exact orientation that maximizes range attains around 12m dispersal range but is highly sensitive to launch conditions and disc morphology. For ballochores with disc-like seeds, the sensitivity of the range-maximizing orientation to seed and launch conditions makes backspin the more attractive and advantageous launch orientation. For *Ruellia ciliatiflora*, the backspin orientation attains a respectable 7m dispersal range, and is robust to moderate perturbations in launch conditions and seed morphologies.

TABLE OF CONTENTS

Acknowledgements	iii
Abstract	iv
Table of Contents	v
List of Illustrations	vi
Chapter I: Introduction	1
1.1 Motivation	1
1.2 Subject Plants	3
1.3 Previous Work	6
1.4 Goals	7
Chapter II: Flight Dynamics of a Thin Spinning Disc	9
2.1 Overview	9
2.2 Launch Mechanics	9
2.3 Coordinate Systems	10
2.4 Aerodynamic Forces	16
2.5 Aerodynamic Torques	23
2.6 Equation of Motion	24
Chapter III: Materials & Methods	26
3.1 Video Analysis & Coefficient Extraction	26
3.2 Numerical Trajectory Simulation	28
Chapter IV: Results & Analysis	32
4.1 Exploratory Simulation & Analysis	32
4.2 Seed Flight Simulations	52
Chapter V: Conclusions and Future Work	61
Bibliography	63

LIST OF ILLUSTRATIONS

<i>Number</i>	<i>Page</i>
1.1 <i>Hura Crepitans</i> , a tropical ballochore capable of launching its seeds at speeds of $70 \frac{m}{s}$. Credit: Hans Hillewaert	3
1.2 <i>Ecballium elaterium</i> , a ballochore with a rather unique seed dispersal mechanism. Credit: Britannica	4
1.3 Phylogeny of family Acanthaceae. Genera in the subcategory Core Acanthaceae utilize ballochory to disperse seeds. Credit: Erin Tripp .	5
1.4 (a) Fruit pods of <i>Ruellia ciliatiflora</i> . Upon ripening, fruits dehisce along vertical failure lines, launching seeds several meters away. Credit: Erin Tripp. (b) Fruit of <i>Ruellia ciliatiflora</i> immediately after dehiscence. Seeds are cradled by hook-like appendages, known as retinacula, which impart momentum during dehiscence. Credit: Erin Tripp. (c) Seeds of <i>R. ciliatiflora</i> with 1mm scale bar. Seeds are disc-like objects approximately 1mm in radius. Credit: Jeremy Wright. Adapted from Cooper.	5
2.1 Diagram of fruit moments after dehiscence. Force is applied by the retinacula on the seed slightly below the seed's center of mass, imparting both linear and angular momentum.	9
2.2 The laboratory frame. The origin is located at the disc's center of mass at time $t = 0$, and gravity acts in the $-\hat{y}$ direction.	11
2.3 In the limit where $(\mathbf{V}) = \hat{x}$, the body frame is equivalent to the lab frame. The orientation of \mathbf{L} is described using a spherical coordinate system with \mathbf{V} serving as the polar axis. The polar and azimuthal angles are θ and ϕ , respectively.	12
2.4 An arbitrary disc orientation. The body frame is used to describe aerodynamic forces, which depend on the orientation of the disc with respect to the flow direction. The orientation of \mathbf{L} is described using a spherical coordinate system with \mathbf{V} serving as the polar axis. The polar and azimuthal angles are θ and ϕ , respectively. The angle α is the angle of attack and is the complement of θ	12
2.5 The body frame is rotated with respect to the laboratory frame about the $y = b_2$ axis by an angle γ	13

2.6	Orientation of the disc with respect to an arbitrary body frame.	14
2.7	Wingtip vortices behind a landing plane cause additional drag, known as induced drag. Credit: NASA Langley Research Center	18
2.8	Lift must lie in the plane defined by \mathbf{L} and \mathbf{V}	19
2.9	a) The wake turbulence behind a nonrotating cylinder is aligned with the freestream flow direction, resulting in no perpendicular force. b) The wake turbulence behind a rotating cylinder is deflected in the direction perpendicular to the freestream velocity, resulting in a net force in the perpendicular direction, which is known as the Magnus force.	21
2.10	(a) Experimentally determined Magnus coefficients of rotating cylinders of varied rotation numbers \mathbf{R} and aspect ratios AR as summarized by Badalamenti. A generally-consistent trend in C_M with \mathbf{R} and AR is apparent. Credit: Badalamenti [2].	22
4.1	Three-dimensional view of backspinning coaster trajectory.	33
4.2	Side view of coaster trajectory when launched near backspin shows total range of approximately 10m.	34
4.3	Bird's eye view of coaster trajectory when launched near backspin ($\phi = 260$) shows that off-horizontal displacement is minimal.	34
4.4	Aerodynamic accelerations experienced by coaster in backspin. . . .	35
4.5	X components of aerodynamic accelerations in backspin. Drag strongly opposes the motion of the disc in the x direction, while the other forces are negligible.	35
4.6	Y components of aerodynamic accelerations in backspin. The Magnus force is always directed upwards. After convergence to backspin, lift is 0.	36
4.7	Z components of aerodynamic accelerations in backspin. The lift force is seen to be the force responsible for displacing the coaster in the z direction, while the other forces are negligible.	36
4.8	Angular dynamics over flight. ϕ quickly converges to backspin ($\phi = 270^\circ$), while α remains quite small over the course of the flight. . . .	37
4.9	Three-dimensional view of sidespinning coaster trajectory.	38
4.10	Side view of sidespinning coaster trajectory. Since the disc is initially oriented with a large planform area, the initial lift is of considerable magnitude. It acts in the positive y direction, pulling the disc above the trajectory that would be experienced by a particle in a vacuum. .	39

4.11	Bird's eye view of coaster trajectory when launched near sidespin shows an appreciable off-horizontal displacement of approximately 3m.	39
4.12	Aerodynamic accelerations experienced by coaster in sidespin.	40
4.13	X components of aerodynamic accelerations in sidespin. Compared to the backspin case, lift in the x direction is significant.	40
4.14	Y components of aerodynamic accelerations in sidespin. Lift is the force responsible for keeping the disc aloft longer than in the backspinning case.	41
4.15	Z components of aerodynamic accelerations in sidespin. Lift is the force responsible for pulling the disc off of the original x direction of motion.	41
4.16	Angular dynamics over sidespin flight. ϕ converges to backspin on the order of 1 second, while α remains quite small over the course of the flight.	42
4.17	Three-dimensional view of topspinning coaster trajectory. Compared to a particle in a vacuum, the topspinning disc has an interesting trajectory, swinging outwards in the $-z$ direction at the apex of the flight before fading back inwards in the . As the disc flips from topspin to sidespin, the lift force pulls the disc in the $-z$ direction. However, as the disc continues flipping from sidespin into backspin, the lift acts in the opposite direction, pulling the disc back in line with the initial trajectory.	43
4.18	Side view of coaster trajectory when launched near topspin shows dispersal range is increased from the backspin orientation, rivaling that of an equivalent-mass particle in a vacuum.	44
4.19	Bird's eye view of coaster trajectory when launched near topspin shows an off-horizontal displacement on the order of 1m.	44
4.20	Net aerodynamic forces on the topspinning disc. Compared to the backspinning case, for the topspinning case, the lift force has an appreciable effect.	45
4.21	X components of aerodynamic accelerations. Drag strongly opposes the motion of the disc in the x direction. The lift force is roughly symmetric in the x direction, integrating the lift over time would show a small net contribution to x acceleration in the $-x$ direction.	45

4.22	<i>Y</i> components of aerodynamic accelerations. The lift force is the primary force responsible for keeping the disc aloft longer than in the backspinning case.	46
4.23	<i>Z</i> components of aerodynamic accelerations. Initially, lift and the Magnus force act to push the coaster in the off-horizontal direction. As ϕ passes 180, the lift force changes direction and acts to pull the coaster back in line with the original flight direction. Much like with the <i>x</i> direction, the symmetry of the lift in the <i>z</i> direction means that the net contribution to overall displacement in the <i>z</i> direction is small.	46
4.24	The angular dynamics of the topspinning coaster. We see the disc's orientation angle ϕ converges to the stable backspinning case on the order of 1.5 seconds.	47
4.25	Three-dimensional trajectories of coasters under a range of ϕ_o from 90° to 270° . Orientations near topspin, but not exactly at topspin, are the range-maximizing orientation.	49
4.26	Range in the direction of initial velocity is shown to be maximized by the coaster launched near topspin.	50
4.27	Vertical view of coaster trajectories shows near-topspin is the range maximizing orientation for the coaster launched with $\beta_o = 40^\circ$	51
4.28	Three-dimensional trajectories of seeds under a range of ϕ_o from 90° to 270° . Orientations around $\phi_o = 110^\circ$ maximize dispersal range, but small changes to the initial orientation result in significant changes to the observed trajectory of the seed.	53
4.29	Range in the direction of initial velocity is shown to be maximized around 110° . Note that many initial orientations perform significantly worse than the backspin case in <i>x</i> displacement.	54
4.30	Vertical view of seed trajectories shows near-topspin is the range maximizing orientation, but small perturbations to initial orientation significantly impact observed trajectory and net displacement range. Many other launch orientations have significant <i>z</i> displacement, which can reduce their overall attained range.	55
4.31	Range in the direction of initial velocity is shown to be maximized around 100° , with some slight dependence on β_o . This is a narrow peak, with slight perturbations in ϕ_o impacting the achieved range significantly. Compare this to backspin at $\phi_o = 270^\circ$. Moderate changes in ϕ_o and β_o do not significantly impact seed dispersal range.	57

- 4.32 $\omega = 1000$ Hz. Range in the direction of initial velocity is shown to be maximized around 115° , with some slight dependence on β_o . The peak near $\phi_o = 115^\circ$ has narrowed compared to the $\omega = 500$ Hz case. The backspin plateau is largely unaffected by the changing ω 58
- 4.33 $\omega = 1500$ Hz. Range in the direction of initial velocity is shown to be maximized around 130° . This optimal peak has narrowed even further with the higher spin rate, making it even more difficult to achieve these larger dispersal ranges, and increasing risk of falling into the valley of failure. 59
- 4.34 Contour showing the ϕ_o that maximizes dispersal range for a given pair of β_o and ω . Height is fixed at 0.75m. The boxed area shows the ranges of β_o and ω that are frequently observed for *R. ciliatiflora* seeds. Within this range, the optimal ϕ_o varies up to 40° . Recall from Figures 4.31 through 4.33 that perturbations greater than 20° can drop the dispersal range from the 12m ridge to the 3m valley. . . 60

Chapter 1

INTRODUCTION

1.1 Motivation

The development of the tools of physical science, engineering, and mathematics has enabled humanity's accomplishment of a countless number of impressive technological feats, but long before the Wright brothers' took to the skies at Kitty Hawk at the turn of the 20th century and Appius Claudius built the first Roman aqueduct in 312 BCE, the physical principles underlying these achievements were well understood by another. From the structural engineering required to keep the immense California redwood upright in the face of gale force winds to the aerodynamics that allow the meager dandelion seed to travel dozens of kilometers, for tens of millions of years, the plant world has had an intimate understanding of complex physical phenomenon that humanity has only begun to piece together within the last few millennia.

Plant species occupy a vast cross section of the natural world, and interesting physics can be found at each and every point. For the fluid dynamicist, an especially interesting area of research is the aerodynamics involved in seed dispersal and flight. The dispersal of a plant's seeds is a short but essential component of its life cycle; successful dispersal of seeds increases the plant's spatial extent, fortifying the genetic line against predation and disease, changing habitat conditions, and other ever-present threats. As such, the selective pressures acting on the seed dispersal process are quite strong, meaning that small perturbations to a plant's seed dispersal technique can greatly impact survivability and propagation, for the better or for worse. These strong selective pressures acting upon seed dispersal result in highly varied and optimized dispersal techniques that provide interesting case studies for the bio-inspired physicist.

Seed dispersal mechanisms are as varied as plants are themselves. Mechanisms of seed dispersal can generally be placed into two broad categories, allochory and autochory. Allochory refers to any seed dispersal process involving external vectors, such as wind (anemochory), water (hydrochory), or animals (zoochory). Such mechanisms are capable of dispersing seeds over impressive distances. Seeds of daisies and other airborne members of the family Asteraceae, for example, can

travel distances on the order of 100km [8], while coconuts and other drift seeds can travel thousands of kilometers across oceans and still remain viable (Edmondson, 1941). Autochory, on the other hand, refers to plants that do not rely on external agents to disperse their seeds. The primary mechanism by which autochores propagate is through ballistic launching of their seeds. This launching mechanism is known as ballistochory or ballochory. Whereas allochores are capable of travelling tens, hundreds, and even thousands of kilometers, the record for largest reported dispersal range among autochores is only around 60m, held by the tropical tree *Tetraberlinia moreliana* [21]. Some plant species utilize a combination of multiple dispersal techniques to distribute their seeds, which is known as diplochory. Spore pods of peat moss, for example, become pressurized and eventually burst, creating a vortex ring that carries spores upwards into stronger winds that distribute the spores over a great range [24].

While it may intuitively seem that larger dispersal ranges would be favorable, there is substantial debate about what particular natural selection mechanisms advantage long range seed dispersal. In their 1982 review, Howe and Smallwood [9] outline some possible explanations of factors favoring long-range dispersal: “The ‘Escape Hypothesis’ implies disproportionate success for seeds that escape the vicinity of the parent, as compared to those that fall nearby. The ‘Colonization Hypothesis’ assumes that habitats change; dispersal in space and time allows a parent’s seeds to take advantage of uncompetitive environments as they open. The ‘Directed Dispersal Hypothesis’ assumes that adaptations ensure that diaspores reach localized sites suitable for establishment.”

These theories explaining selection in favor of long-range dispersal are reasonable, but the elusive nature of evolutionary biology makes it difficult to conclusively attribute observed dispersal behavior to any particular selective pressure. The orders of magnitude difference in seed dispersal ranges between allochores and autochores is suggestive of the idea that the selective pressures acting upon seed dispersal may be collectively favoring some parameter or combination of parameters other than pure dispersal range. If range were the only parameter of interest, why should ballochory have evolved when allochory is orders of magnitude more effective? A rigorous characterization of the dynamics of seed dispersal in a range of allochores may provide useful insight into this question.

1.2 Subject Plants

While ballochory is a comparatively rare dispersal technique, ballochores are still found across a wide range of habitats and plant families, and there is impressive diversity in the specific implementation of dispersal mechanisms across ballochores. *Hura crepitans* is a tropical tree found in North and South America whose fruits explode when ripe, launching seeds with a velocity of approximately 70m/s [23]. Many ballochores rely on a similar launch mechanism, but others employ more unique techniques. For example, *Ecballium elaterium*, commonly known as the “squirting cucumber,” uses osmosis to pressurize a cavity containing seeds. A cap at the tip of the fruit eventually fails, causing a forceful discharge of fluid containing the plant’s seeds out of the tip of the fruit [14]. The fruits of *Hamamelis mollis* employ a similar launch mechanism, but instead of fluid pressure, the squeeze is entirely mechanical. In much the same way one can launch a watermelon seed by squeezing it tightly between the fingers, the football-shaped seeds of *H. mollis* are squeezed from the rear, launching with velocity greater than 10m/s and a stabilizing spin about their axes of symmetry, akin to that of a bullet shot from a rifle [17].



Figure 1.1: *Hura Crepitans*, a tropical ballochore capable of launching its seeds at speeds of $70 \frac{m}{s}$. Credit: Hans Hillewaert



Figure 1.2: *Ecballium elaterium*, a ballochore with a rather unique seed dispersal mechanism. Credit: Britannica

Acanthaceae is a large, diverse family of flowering plants whose species number over 4000 across more than 200 genera. There is considerable diversity in traits within Acanthaceae, including flower appearance, pollen grains, and leaves. Physical plant size ranges from small shrubbery to trees. The family is subcategorized according to their seed dispersal mechanism; members of the core Acanthaceae subgroup are ballochores, while others utilize different dispersal mechanisms. *Ruellia* is a genus contained within the core Acanthaceae subgroup that has been studied extensively in recent years, [7], [15], [20]. Members of *Ruellia* have fruits that explosively dehisce upon contact with water, a property known as hygrochacy. The fruits of these *Ruellia* species consist of a small capsule that contains a small number of seeds connected to hook-like structures known as retinacula or jaculators, pictured below for *Ruellia ciliatiflora*. Upon fruit dehiscence, these jaculators deliver an impulse to their corresponding seeds, launching them several meters away from their parent [25]. The primary species used in this thesis is *Ruellia ciliatiflora*.

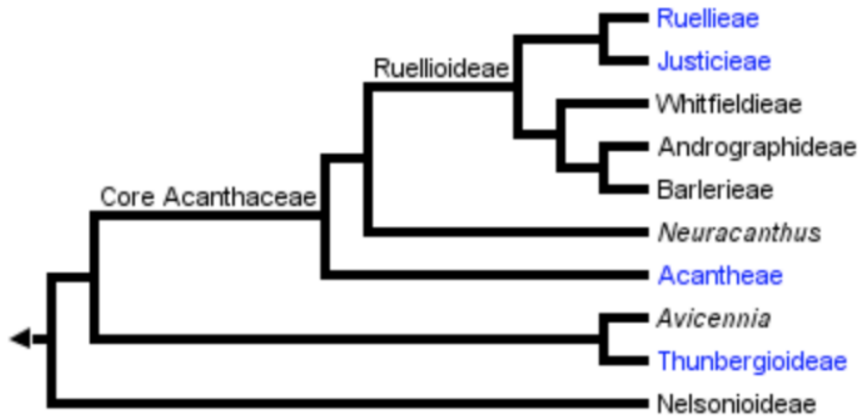


Figure 1.3: Phylogeny of family Acanthaceae. Genera in the subcategory Core Acanthaceae utilize ballochory to disperse seeds. Credit: Erin Tripp



Figure 1.4: (a) Fruit pods of *Ruellia ciliatiflora*. Upon ripening, fruits dehisce along vertical failure lines, launching seeds several meters away. Credit: Erin Tripp. (b) Fruit of *Ruellia ciliatiflora* immediately after dehiscence. Seeds are cradled by hook-like appendages, known as retinacula, which impart momentum during dehiscence. Credit: Erin Tripp. (c) Seeds of *R. ciliatiflora* with 1mm scale bar. Seeds are disc-like objects approximately 1mm in radius. Credit: Jeremy Wright. Adapted from Cooper.

1.3 Previous Work

A significant number of studies comparing seed dispersal techniques within the major dispersal mechanism categories exist; anemochores [4], ballochores [15] [6] [17], hydrochores [10], and diplochores [5]. Comparatively little work, however, has been conducted comparing the evolution of dispersal techniques across the primary dispersal mechanism categories, primarily due to the complexity of various selective pressures as they act to influence seed dispersal. One of the few studies in this area is a broad analysis of Central European flora that compared characteristic dispersal distances across the major dispersal mechanism categories, [22]. Analysis of the dynamics of seed dispersal in ballochores will provide a foundation supporting targeted study into the comparative biology and evolution of different dispersal mechanisms across the plant kingdom.

Compared to allochores, autochores are outnumbered in the natural world but are still well-studied. Their simplicity and lack of reliance on inconsistent external agents to disperse their seeds makes them a comparatively simpler subject for a study of seed dispersal evolution. This fact has been exploited in previous studies of seed dispersal. For example, it has been shown that the internal structure of ballochore fruits has evolved in such a way as to maximize energy delivered to the seed upon launch [25], and that initial launch angle in many ballochores is near the ideal range-maximizing angle for a projectile experiencing aerodynamic drag [21] [25]). Species in the genus *Ruellia* have been the subject of multiples studies in recent years that have revealed fascinating insights into the physics of the dispersal of their seeds. Seeds of *Ruellia cilitatiflora*, pictured in Figure 1.3(c), have been observed flying with rotation rates as high 1660 Hz, one of the largest rotation rates in the biological world [6]. This backspin was shown by Cooper to stabilize the seed in a low-drag orientation, thus increasing the range of the seed as compared to a bluff projectile of equivalent mass and volume [7].

On the physical side, studies detailing aspects of the flight of discuses have been released [6] [16] [18], though none of these papers fully consider the effects of disc angular momentum on dynamics of flight nor do they fully characterize resulting three-dimensional trajectories for the parameter space occupied by *Ruellia* seeds. Most recently, approximate flight trajectories for beer coasters, which are essentially thin, spinning discs, were derived using a Lagrangian approach [16]. For this thesis, deriving the equation of motion of thin, spinning discs using a Newtonian framework provides a check on the validity of Ostmeyer's results for the general

dynamics of a thin, spinning disc. Additionally, studies of the seeds of Ruellia, with their high rates of rotation, vertical orientations, and intermediate Reynolds number, are related to these studies, but occupy a different part of parameter space, and are therefore interesting subjects of study in their own right.

1.4 Goals

The fluid mechanics problem inspired by the flight of Ruellia seeds is to fully characterize the dynamics of spinning discs traveling in a fluid medium. This problem cannot be solved using solely mathematical tools, as the governing equations – the Navier-Stokes Equations – are impossible to solve analytically except under the most basic of flow conditions. Solutions to Navier-Stokes are so difficult, in fact, that a proof (or disproof) of the existence of unique, smooth solutions to the Navier-Stokes equations is worth a cool \$1,000,000 courtesy of the Clay Mathematics Institute as part of the Millennium Prize.

The engineer's crutch of computational fluid dynamics (CFD) codes, while theoretically capable of simulating the trajectory of flying seeds, is also untenable for the problem at hand. Fluids solvers function by taking a user-defined flow domain and boundary conditions, first discretizing the domain into finite elements, then iteratively approximating and refining solutions to the Navier-Stokes and other governing equations in each of the domain elements. Accurate approximations require finely resolved meshes with small element sizes, especially near fluid-solid interfaces if viscous and frictional effects are to be included. For many analyses, the meshing process is as, if not more, computationally demanding than the actual solving of the Navier-Stokes equations. For flows with moving or deforming boundary conditions, as in the case of a free projectile moving in a fluid, a new mesh must be constructed for each time step of the simulation, increasing the computational demand by several orders of magnitude. Ultimately the computational cost of accurately simulating the real flow around a moving projectile is too large for CFD to serve as a useful tool to apply to such a problem.

The impossibility of direct application of the Navier-Stokes equations and the impracticality of applying CFD codes leave us with only experimentation and approximate analytical methods as practical tools for analyzing the motion of ballochore seeds, and projectiles travelling in a fluid medium more generally. Seeds of the Ruellia genus can be modelled as thin, flat discs, launched with an initial rate of rotation about their axes of symmetry. Results from potential flow theory, which

considers flows in the limit of no viscosity or friction, and thin airfoil theory, which describes flows around thin bodies, can be used to determine approximate forms of the aerodynamic forces acting on the moving disc. These forces can be used to construct an equation of motion that fully describes the three-dimensional trajectory of a thin, spinning disc flying in a fluid medium and can be checked against Cooper's and Ostemeyer's derivations. This equation can be solved numerically with varied seed dimensions and launch parameters to explore parameter space and determine optimal conditions to maximize dispersal range for a given seed. These ideal conditions can then be compared to observed launch parameters and seed dimensions for a given species to determine the optimality of that species' dispersal technique.

Chapter 2

FLIGHT DYNAMICS OF A THIN SPINNING DISC

2.1 Overview

In this chapter, an equation of motion will be developed for a thin, spinning disc travelling through air. We first characterize the launching mechanism of *Ruellia ciliatiflora* fruits. We then define two coordinate systems in which we will analyze the disc's behavior. Finally, we characterize the aerodynamic forces and torques experienced by the disc as it travels through the fluid medium. The results of these analyses are used to construct a system of five coupled nonlinear differential equations that describes the motion of the disc.

2.2 Launch Mechanics

The seeds of *ciliatiflora* and other species in the genus Ruellia are oriented within the fruit such that, upon fruit dehiscence, a force is applied below the seeds' center of mass, per Figure 2.1. This off-center force provides both translational and rotational motion to the seeds, yielding launch velocities and rotation rates around 10 m/s and 1000 Hz, respectively, for *R. ciliatiflora*.

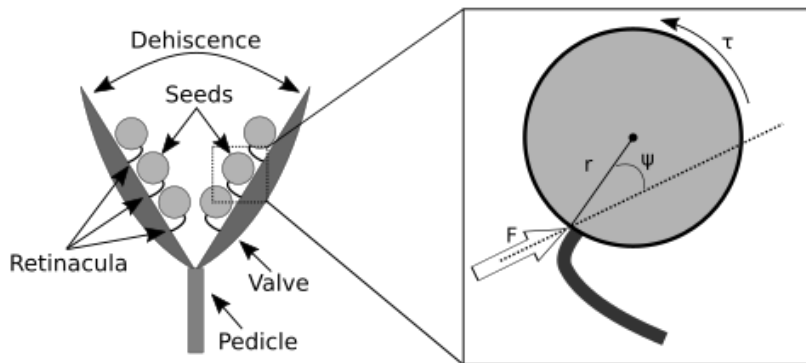


Figure 2.1: Diagram of fruit moments after dehiscence. Force is applied by the retinacula on the seed slightly below the seed's center of mass, imparting both linear and angular momentum.

The velocity of the disc $|\mathbf{V}|$ can be expressed in terms of the linear momentum p and mass m , and the angular velocity of the disc ω can be expressed in terms of angular momentum \mathbf{L} and moment of inertia I .

$$|\mathbf{V}| = \frac{p}{m} \quad (2.1)$$

$$|\omega| = \frac{L}{I} = \frac{pr \sin(\psi)}{\eta mr^2} \quad (2.2)$$

In the last step, we express the angular momentum in terms of linear momentum, radius r , and contact angle ψ , and substitute in for the moment of inertia $I = \eta mr^2$. The term η is a shape-dependent dimensionless constant equal to 1/2 for a homogenous disc rotating about its axis of symmetry and 2/5 for a homogenous sphere rotating about any axis. A dimensionless rotation number, also referred to as spin parameter, comparing the relative magnitudes of the linear and angular velocities can be defined as $\mathbf{R} = \frac{\omega r}{|\mathbf{V}|}$. Substituting equations (2.1) and (2.2) into this definition yields

$$\mathbf{R} = \frac{\omega r}{|\mathbf{V}|} = \frac{pr^2 |\sin(\psi)|}{\eta mr^2} * \frac{m}{p} = \frac{|\sin(\psi)|}{\eta} \quad (2.3)$$

We find that the rotation number \mathbf{R} depends only on the contact angle ψ and the dimensionless moment of inertia η . Taking the thin disc value of $\eta = 1/2$, we find \mathbf{R} is bounded by $0 \leq \mathbf{R} \leq 2$. We can combine this bound with the average launch velocities and radii of *R. ciliatiflora* seeds to place an upper bound on the angular velocity achievable by this launch mechanism

$$|\omega| = \frac{|\mathbf{V}|\mathbf{R}}{r} \approx \frac{10 \frac{m}{s} * 2}{0.001 m} \approx 20,000 \frac{rad}{s} \approx 3200 Hz \quad (2.4)$$

2.3 Coordinate Systems

To characterize the flight dynamics of a thin, spinning disc, an overview of coordinate systems is in order. There are two primary coordinate systems that are used to describe the disc's behavior: the laboratory frame, which serves as the absolute reference frame in which we seek to define the disc's equation of motion, and the body frame, a useful formulation we can exploit to simplify the analysis of the aerodynamic forces and moments experienced by the disc.

The Laboratory Frame

Define the origin of the laboratory frame as the location of the center of mass of the disc at time $t = 0$. Let the frame be oriented such that $dir(\mathbf{g}) = -\hat{y}$, then

define the x and z axes such that the laboratory frame is a right-handed coordinate system. The velocity vector \mathbf{V} of the disc is defined with respect to the laboratory frame using a spherical coordinate system with x taken to be the polar axis. The angle β is the polar angle, giving the vertical inclination of \mathbf{V} with respect to the horizontal xz plane, and the angle γ is the azimuthal angle of \mathbf{V} , relative to the x axis.

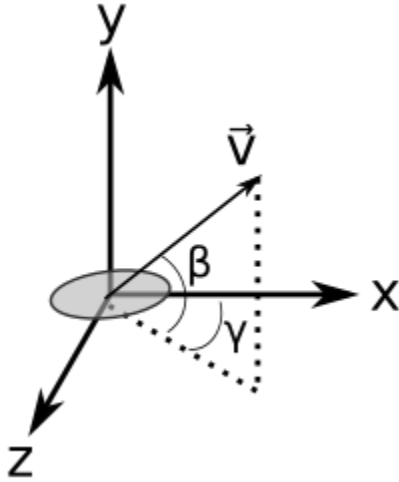


Figure 2.2: The laboratory frame. The origin is located at the disc's center of mass at time $t = 0$, and gravity acts in the $-\hat{y}$ direction.

The Body Frame

Since aerodynamic forces depend on the orientation of an object with respect to the relative wind, we define our second coordinate frame, the body frame, with respect to the velocity vector \mathbf{V} . Given the axisymmetry of a thin disc, we can uniquely describe its orientation in space using only its normal vector \mathbf{n} . We assume that the angular momentum vector \mathbf{L} is always colinear with \mathbf{n} . We seek to describe the orientation of \mathbf{L} with respect to \mathbf{V} , which in turn is described with respect to the laboratory frame.

We set the first axis of the body frame b_1 such that it is aligned with the instantaneous velocity vector \mathbf{V} . Then orient the remaining body frame axes b_2 and b_3 such that, in the limit where $dir(\mathbf{V}) = \hat{x}$, the body frame is equivalent to the laboratory frame, as shown in Figure 2.3. To describe the angular momentum vector \mathbf{L} with respect to the velocity vector \mathbf{V} , take \mathbf{V} to be the polar axis of a spherical coordinate system. Then, let θ be the polar angle of \mathbf{L} and ϕ be the azimuthal angle about \mathbf{V} , zeroed at $-\hat{b}_2$. The components of \mathbf{L} in the body frame are given by

$$L_{b1} = |\mathbf{L}| \cos(\theta) \quad (2.5)$$

$$L_{b2} = -|\mathbf{L}| \sin(\theta) \cos(\phi) \quad (2.6)$$

$$L_{b3} = -|\mathbf{L}| \sin(\theta) \sin(\phi) \quad (2.7)$$

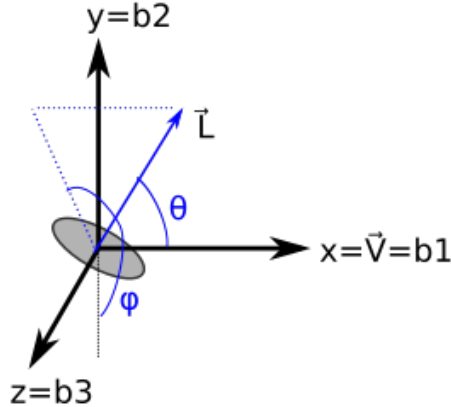


Figure 2.3: In the limit where $(\mathbf{V}) = \hat{x}$, the body frame is equivalent to the lab frame. The orientation of \mathbf{L} is described using a spherical coordinate system with \mathbf{V} serving as the polar axis. The polar and azimuthal angles are θ and ϕ , respectively.

Over the course of the flight, the velocity of the disc will vary, causing changes in the orientation of the body frame relative to the laboratory frame. An arbitrary body frame, along with the relevant angles, is given in Figure 2.4. Using the angles β and γ , which describe the orientation of \mathbf{V} with respect to the laboratory frame, we can generalize the representation of the angular momentum \mathbf{L} for arbitrary orientations of \mathbf{V} .

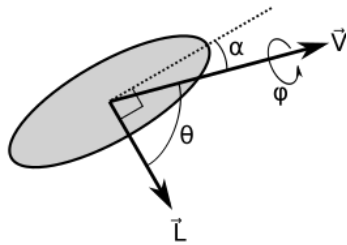


Figure 2.4: An arbitrary disc orientation. The body frame is used to describe aerodynamic forces, which depend on the orientation of the disc with respect to the flow direction. The orientation of \mathbf{L} is described using a spherical coordinate system with \mathbf{V} serving as the polar axis. The polar and azimuthal angles are θ and ϕ , respectively. The angle α is the angle of attack and is the complement of θ .

As shown in Figure 2.2, the direction of \mathbf{V} with respect to the laboratory frame can be described using two angles β and γ . Given changes in β and γ , the body frame will transform to maintain the alignment of b_1 with \mathbf{V} . We take β and γ to be two Euler angles that can be used to uniquely define the orientation of the body frame with respect to the lab frame. While the most general representation of a body's orientation in space would require a third Euler angle, the axisymmetry of the disc reduces the dimensionality of the disc's orientation to two angles. The general conversion between the body frame and the laboratory frame is given by

$$\mathbf{X}_{lab} = \mathbf{M}_{rot} \mathbf{X}_{body} \quad (2.8)$$

where \mathbf{X}_{lab} is the representation of a vector \mathbf{X} in the components of the body frame, \mathbf{X}_{body} is the representation of \mathbf{X} in the laboratory frame, and \mathbf{M}_{rot} is a 3×3 matrix known as a rotation matrix. To construct the rotation matrix, we use the Euler angle formalism, in which a unique body frame is constructed via sequential rotations about certain axes. Each individual rotation has an associated rotation matrix $\mathbf{M}(\theta)$, which can be matrix multiplied in reverse order to construct the overall rotation matrix \mathbf{M}_{rot} . Consider the lab-body frame relationship as shown in Figure 2.3. Now, rotate the body frame through an angle γ about the $b_2 = y$ axis, per 2.5.

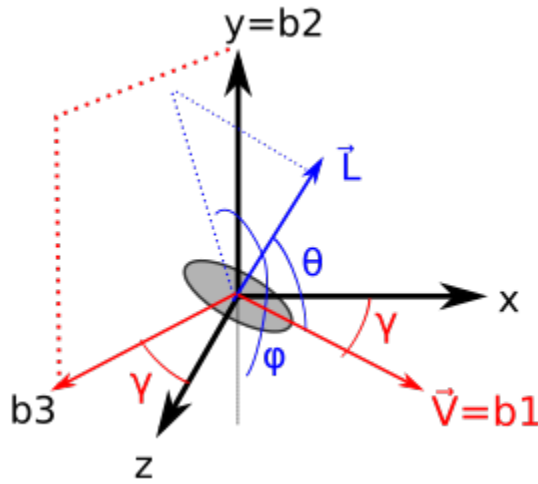


Figure 2.5: The body frame is rotated with respect to the laboratory frame about the $y = b_2$ axis by an angle γ .

The rotation matrix for this single-axis rotation is given by

$$\mathbf{M}(\gamma) = \begin{pmatrix} \cos(\gamma) & 0 & \sin(\gamma) \\ 0 & 1 & 0 \\ -\sin(\gamma) & 0 & \cos(\gamma) \end{pmatrix}$$

(2.9)

Now, rotate this new body frame through an angle β about the new b_3 axis, per Figure 2.6

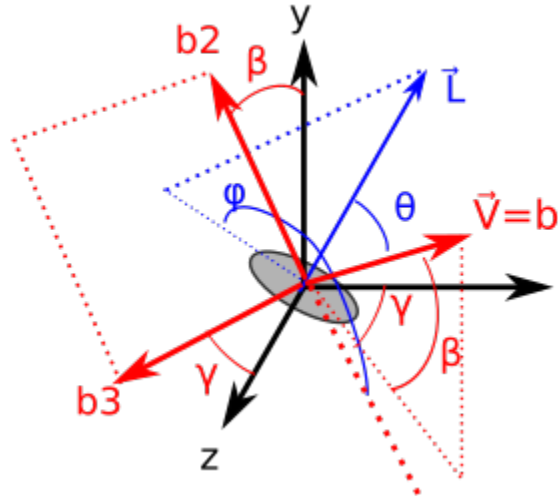


Figure 2.6: Orientation of the disc with respect to an arbitrary body frame.

The rotation matrix for this second single-axis rotation is given by

$$\mathbf{M}(\beta) = \begin{pmatrix} \cos(\beta) & \sin(\beta) & 0 \\ -\sin(\beta) & \cos(\beta) & 0 \\ 0 & 0 & 1 \end{pmatrix} \quad (2.10)$$

To get the overall rotation matrix \mathbf{M}_{rot} that converts a vector from the body frame to the laboratory frame, we multiply these two individual rotation matrices in reverse order

$$\begin{aligned}
\mathbf{M}_{rot} &= \begin{pmatrix} \cos(\beta) & \sin(\beta) & 0 \\ -\sin(\beta) & \cos(\beta) & 0 \\ 0 & 0 & 1 \end{pmatrix} * \begin{pmatrix} \cos(\gamma) & 0 & \sin(\gamma) \\ 0 & 1 & 0 \\ -\sin(\gamma) & 0 & \cos(\gamma) \end{pmatrix} \\
&= \begin{pmatrix} \cos(\beta)\cos(\gamma) & -\sin(\beta) & -\cos(\beta)\sin(\gamma) \\ \sin(\beta)\cos(\gamma) & \cos(\beta) & -\sin(\beta)\cos(\gamma) \\ \sin(\gamma) & 0 & \cos(\gamma) \end{pmatrix}
\end{aligned} \tag{2.11}$$

Given the vector $\mathbf{L}_{body} = [L_{b1}, L_{b2}, L_{b3}]$ defined with respect to the body frame via the angles θ and ϕ (equations (2.5) through (2.7)), we transform the representation of \mathbf{L} to the laboratory frame by

$$\begin{aligned}
\mathbf{L}_{lab} &= \mathbf{M}_{rot}\mathbf{L}_{body} \\
&= \begin{pmatrix} \cos(\beta)\cos(\gamma) & -\sin(\beta) & -\cos(\beta)\sin(\gamma) \\ \sin(\beta)\cos(\gamma) & \cos(\beta) & -\sin(\beta)\cos(\gamma) \\ \sin(\gamma) & 0 & \cos(\gamma) \end{pmatrix} * \begin{pmatrix} |\mathbf{L}|\cos(\theta) \\ -|\mathbf{L}|\sin(\theta)\cos(\phi) \\ -|\mathbf{L}|\sin(\theta)\sin(\phi) \end{pmatrix} \\
&= |\mathbf{L}| \begin{pmatrix} \cos(\beta)\cos(\gamma)\cos(\theta) + \sin(\beta)\sin(\theta)\cos(\phi) + \cos(\beta)\sin(\gamma)\sin(\theta)\sin(\phi) \\ \sin(\beta)\cos(\gamma)\cos(\theta) - \cos(\beta)\sin(\theta)\cos(\phi) + \sin(\beta)\sin(\gamma)\sin(\theta)\sin(\phi) \\ \sin(\gamma)\cos(\theta) - \cos(\gamma)\sin(\theta)\sin(\phi) \end{pmatrix}
\end{aligned} \tag{2.12}$$

The above equation converts the vector $\mathbf{L}_{body} = [L_{b1}, L_{b2}, L_{b3}]$ defined with respect to the laboratory frame to the vector $\mathbf{L}_{lab} = [L_x, L_y, L_z]$ defined with respect to the body frame. Recall that \mathbf{L} was originally defined with respect to the velocity vector \mathbf{V} using the angles θ and ϕ , and the velocity vector was in turn defined with respect to the laboratory frame using the angles β and γ . α is the angle between the chordline of the disc and the relative wind, and θ and α are complementary angles, that is, $\alpha + \theta = 90$. Also, we can express the velocity angles β and γ in terms of their components in the laboratory frame.

$$\sin(\beta) = \frac{V_y}{|\mathbf{V}|} \tag{2.13}$$

$$\cos(\beta) = \frac{\sqrt{V_x^2 + V_z^2}}{|\mathbf{V}|} \tag{2.14}$$

$$\sin(\gamma) = \frac{V_z}{\sqrt{V_x^2 + V_z^2}} \quad (2.15)$$

$$\cos(\gamma) = \frac{V_x}{\sqrt{V_x^2 + V_z^2}} \quad (2.16)$$

Since α and θ are complementary, $\alpha = \frac{\pi}{2} - \theta$. By trigonometry of complementary angles, $\sin(\theta) = \cos(\alpha)$ and $\cos(\theta) = \sin(\alpha)$. Reexpressing equation (2.12) in terms of α and the above component-wise velocity expressions yields

$$L_x = \frac{V_x}{|\mathbf{V}|} \sin(\alpha) + \frac{V_y}{|\mathbf{V}|} \cos(\alpha) \cos(\phi) + \frac{V_z}{|\mathbf{V}|} \cos(\alpha) \sin(\phi) \quad (2.17)$$

$$L_y = \frac{V_y}{|\mathbf{V}|} \frac{V_x}{\sqrt{V_x^2 + V_z^2}} \sin(\alpha) - \frac{\sqrt{V_x^2 + V_z^2}}{|\mathbf{V}|} \cos(\alpha) \cos(\phi) + \frac{V_y}{|\mathbf{V}|} \frac{V_z}{\sqrt{V_x^2 + V_z^2}} \cos(\alpha) \sin(\phi) \quad (2.18)$$

$$L_z = \frac{V_z}{\sqrt{V_x^2 + V_z^2}} \sin(\alpha) - \frac{V_x}{\sqrt{V_x^2 + V_z^2}} \cos(\alpha) \sin(\phi) \quad (2.19)$$

Equations (2.17) through (2.19) are the final component-wise expressions of \mathbf{L} in the laboratory frame given a velocity $\mathbf{V} = [V_x, V_y, V_z]$ defined with respect to the lab frame via the angles β and γ , and an angular momentum \mathbf{L} defined with respect to \mathbf{V} via the angles α and ϕ .

2.4 Aerodynamic Forces

Any object moving through a fluid is subject to a force resulting from the displacement of the fluid in the path of the object and frictional effects occurring at the fluid-solid interface. This net aerodynamic force is split into two components parallel and perpendicular to the direction of the flow velocity, known as drag and lift, respectively. The drag force can be further subcategorized based on its physical origin. Viscous drag arises from frictional forces acting between the fluid and solid, and scales linearly with flow velocity. Form drag is due to the object continually needing to accelerate the mass of fluid with which it collides, and scales as the square of the velocity. When the fluid in question is air at standard conditions, the form drag dominates the overall drag force for all but the slowest flows, so the linear drag term can safely be ignored. An additional force that occurs with spinning bodies is the Magnus force, the physical origin of which is the viscous displacement of the wake turbulence behind bluff bodies.

Lift & Drag

It is conventional to represent both the lift and the drag forces as functions of the flow dynamic pressure $q = \frac{1}{2}\rho|\mathbf{V}|^2$, where ρ is the fluid density, a characteristic area A , and a unitless aerodynamic coefficient C . The resulting lift and drag forces are given by

$$|\mathbf{F}_L| = \frac{C_L}{2}\rho|\mathbf{V}|^2A \quad (2.20)$$

$$|\mathbf{F}_D| = \frac{C_D}{2}\rho|\mathbf{V}|^2A \quad (2.21)$$

For most bodies, the characteristic area A for the drag force is the frontal area, given by $A = (\pi r^2 \sin(\alpha) + 2rd \cos(\alpha))$, whereas the characteristic area for the lift force is the planform area, given $A = \pi r^2 \cos(\alpha)$, for a disc of radius r , thickness d , at angle of attack α . The aerodynamic coefficients C_L and C_D vary with angle of attack α . For a thin, flat plate, the lift coefficient is a function of α [3].

$$C_L = 2\pi \sin(\alpha) \quad (2.22)$$

Substituting this expression into equation (2.20), the resulting lift force is given by

$$|\mathbf{F}_L| = \frac{\pi^2 r^2 \rho}{2} |\mathbf{V}|^2 \sin(2\alpha) \quad (2.23)$$

where we use the double angle identity $\sin(\alpha) \cos(\alpha) = \frac{1}{2} \sin(2\alpha)$.

The relationship between α and C_D is more complex. Video analysis of flying *R. ciliatiflora* seeds reveals a drag coefficient of approximately $C_D = .301$ [19]. There is an additional source of drag known as induced drag that results from three dimensional airflow effects over finite wings. Any lifting body is subject to induced drag. Lift over a wing is generated by the creation of a vertical pressure gradient with high pressure underneath the wing and low pressure above. Near the tips of wings, the high pressure below the wing "leaks out" around the wingtip, creating vortices that increase the drag experienced by the body, as seen in Figure 2.7. The induced drag is typically expressed as an additive component $C_{D,induced}$ to the original drag coefficient C_D

$$C_{D,induced} = \frac{C_L^2}{\pi AR e} \quad (2.24)$$

where AR is the aspect ratio of the lifting body and e is an efficiency factor slightly less than 1. The aspect ratio is equal to the square of the wingspan divided by wing area. The wingspan is equal to the diameter $2r$. This yields an aspect ratio of $AR = \frac{(2r)^2}{\pi * r^2} = \frac{4}{\pi}$. An elliptical wing has an efficiency factor of 1, and a rectangular wing has an efficiency factor of .7 [11]. It is unclear how these values can be used to estimate the efficiency factor of the circular wing, further work is needed here. For now, we choose an intermediate efficiency factor of 0.5 for the circular wing and substitute into equation (2.21)

$$\mathbf{F}_D = -\frac{(0.301 + 2\pi^2 \sin(\alpha)^2)}{2} (\pi r^2 |\sin(\alpha)| + 2dr |\cos(\alpha)|) \rho |\mathbf{V}|^2 \hat{\mathbf{V}} \quad (2.25)$$



Figure 2.7: Wingtip vortices behind a landing plane cause additional drag, known as induced drag. Credit: NASA Langley Research Center

Equations (2.23) and (2.25) give the components of the net aerodynamic force in perpendicular and parallel directions to the freestream, respectively. The direction of the drag force is uniquely defined by (2.25), acting to oppose the motion of the object. We can express the drag force in component form using equations (2.13) through (2.16)

$$\begin{aligned} F_{Dx} &= |\mathbf{F}_D| \sin(\alpha) \cos(\beta) \cos(\gamma) \\ &= -\frac{(0.301 + 2\pi^2 \sin(\alpha)^2)}{2} (\pi r^2 |\sin(\alpha)| + 2dr |\cos(\alpha)|) \rho |\mathbf{V}| V_x \end{aligned} \quad (2.26)$$

$$\begin{aligned} F_{Dy} &= |\mathbf{F}_D| \sin(\alpha) \cos(\beta) \cos(\gamma) \\ &= -\frac{(0.301 + 2\pi^2 \sin(\alpha)^2)}{2} (\pi r^2 |\sin(\alpha)| + 2dr |\cos(\alpha)|) \rho |\mathbf{V}| V_y \end{aligned} \quad (2.27)$$

$$\begin{aligned} F_{Dz} &= |\mathbf{F}_D| \sin(\alpha) \cos(\beta) \cos(\gamma) \\ &= -\frac{(0.301 + 2\pi^2 \sin(\alpha)^2)}{2} (\pi r^2 |\sin(\alpha)| + 2dr |\cos(\alpha)|) \rho |\mathbf{V}| V_z \end{aligned} \quad (2.28)$$

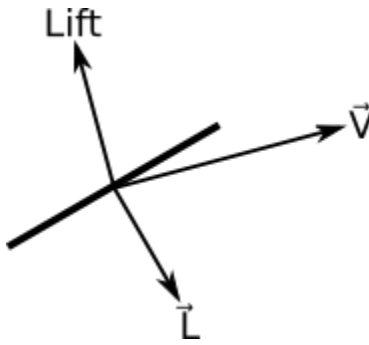


Figure 2.8: Lift must lie in the plane defined by \mathbf{L} and \mathbf{V} .

The lift force, however, is not uniquely defined by (2.23). The lift force must act perpendicularly to the flow direction, but in the three-dimensional case, that constraint only limits the direction of lift to a plane; an additional constraint is needed to fully specify the direction of lift. That final constraint can be obtained by a qualitative discussion of the symmetry of the disc. Consider the case where \mathbf{L} and \mathbf{V} lie in the plane of the page, as shown in Figure 2.8. There is no physical mechanism by which the lift should be able to act out of this plane. Therefore, the lift vector must lie in the plane defined by \mathbf{L} and \mathbf{V} . The three constraints on the lift are expressed mathematically as

$$\mathbf{F}_L \cdot \mathbf{V} = 0 \quad (2.29)$$

$$\mathbf{F}_L \cdot (\mathbf{V} \times \mathbf{L}) = 0 \quad (2.30)$$

$$|\mathbf{F}_L| = \frac{\pi^2 r^2 \rho}{2} \sin(2\alpha) |\mathbf{V}|^2 \quad (2.31)$$

This set of constraints can be expressed in component form as

$$F_{Lx}V_x + F_{Ly}V_y + F_{Lz}V_z = 0 \quad (2.32)$$

$$F_{Lx}(V_yL_z - V_zL_y) + F_{Ly}(V_zL_x - V_xL_z) + F_{Lz}(V_xL_y - V_yL_x) = 0 \quad (2.33)$$

$$\sqrt{F_{Lx}^2 + F_{Ly}^2 + F_{Lz}^2} = \frac{\pi^2 r^2 \rho}{2} \sin(2\alpha)(V_x^2 + V_y^2 + V_z^2) \quad (2.34)$$

Equations (2.32) through (2.34) represent a system of three unknowns (F_x, F_y, F_z) in three equations. They can be solved to yield the three components of the lift force \mathbf{F}_L in the laboratory frame.

$$F_{Lx} = \frac{\frac{\pi^2 r^2 \rho}{2} \sin(2\alpha) |\mathbf{V}|^2 (L_y V_x V_y + L_z V_x V_z - L_x (V_y^2 + V_z^2))}{\sqrt{V^2 (L_x^2 (V_y^2 + V_z^2) + L_y^2 (V_x^2 + V_z^2) + L_z^2 (V_x^2 + V_y^2) - 2 L_x L_z V_x V_z - 2 L_y V_y (L_x V_x + L_z V_z))}} \quad (2.35)$$

$$F_{Ly} = -\frac{\frac{\pi^2 r^2 \rho}{2} \sin(2\alpha) |\mathbf{V}|^2 (L_y (V_x^2 + V_z^2) - V_y (L_x V_x + L_z V_z))}{\sqrt{V^2 (L_x^2 (V_y^2 + V_z^2) + L_y^2 (V_x^2 + V_z^2) + L_z^2 (V_x^2 + V_y^2) - 2 L_x L_z V_x V_z - 2 L_y V_y (L_x V_x + L_z V_z))}} \quad (2.36)$$

$$F_{Lz} = -\frac{\frac{\pi^2 r^2 \rho}{2} \sin(2\alpha) |\mathbf{V}|^2 (L_z (V_x^2 + V_y^2) - V_z (L_x V_x + L_y V_y))}{\sqrt{V^2 (L_x^2 (V_y^2 + V_z^2) + L_y^2 (V_x^2 + V_z^2) + L_z^2 (V_x^2 + V_y^2) - 2 L_x L_z V_x V_z - 2 L_y V_y (L_x V_x + L_z V_z))}} \quad (2.37)$$

The third constraint, equation (2.34), introduces a sign ambiguity in the components of \mathbf{F}_L . As written, the solution set is valid for $-90 < \alpha < 90$. A second solution with opposite signs exists for angles of attack outside of this range. However, α remains within a small range centered on 0 for the entirety of the flight, meaning the solution shown above is the only solution of interest.

Magnus Effect

An additional aerodynamic force that applies only to spinning bodies is the Magnus force. In the inviscid limit, the Magnus force can be explained by considering a rotating cylinder in a uniform flow. For the backspinning cylinder, the top surface of the cylinder moves in the direction of the freestream flow, adding slightly to the overall flow velocity along the top surface of the cylinder. By Bernoulli's Principle, the faster flow along the top surface of the cylinder decreases the pressure relative to the bottom surface, resulting in an upwards force acting on the backspinning cylinder. The situation is reversed for the topspinning cylinder, where the flow along the top surface of the cylinder is slowed relative to the bottom surface, increasing the pressure on the top surface and imparting a downwards force. In reality, the Magnus force is dominated by viscous effects. The true source of the Magnus force is a spin-induced deflection of the wake turbulence behind the cylinder, per Figure 2.9.

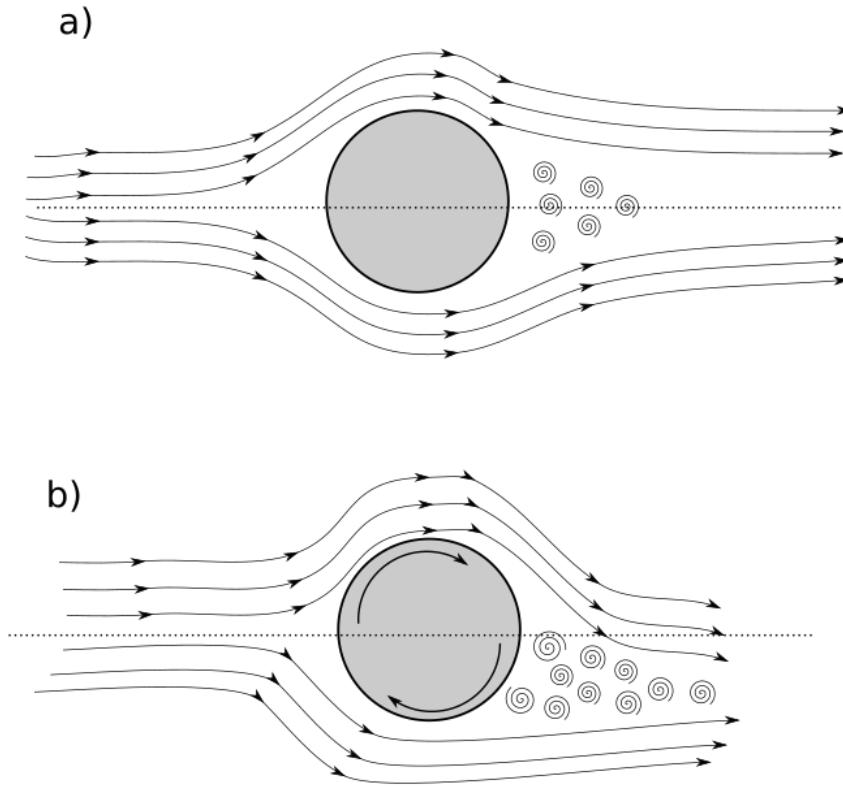


Figure 2.9: a) The wake turbulence behind a nonrotating cylinder is aligned with the freestream flow direction, resulting in no perpendicular force. b) The wake turbulence behind a rotating cylinder is deflected in the direction perpendicular to the freestream velocity, resulting in a net force in the perpendicular direction, which is known as the Magnus force.

Similarly to the lift and drag forces, the conventional representation of the Magnus force is given by

$$F_M = \frac{C_M}{2} \rho |\mathbf{V}|^2 A \quad (2.38)$$

where C_M is a dimensionless coefficient and A is the surface area of the cylinder exposed to the flow. The Magnus force acts perpendicularly to both the rotation and velocity of the body, in the direction given by $\hat{\mathbf{L}} \times \hat{\mathbf{V}}$. C_M is dependent on the rotation number \mathbf{R} and the ratio of the cylinder's diameter to its length, known as cylinder aspect ratio. The Magnus coefficient is also impacted by the material of the cylinder and its surface roughness. Magnus coefficients for a variety of cylinder aspect ratios and rotation numbers have been experimentally measured [2]. A summary of these relationships is given in Figure 2.10.

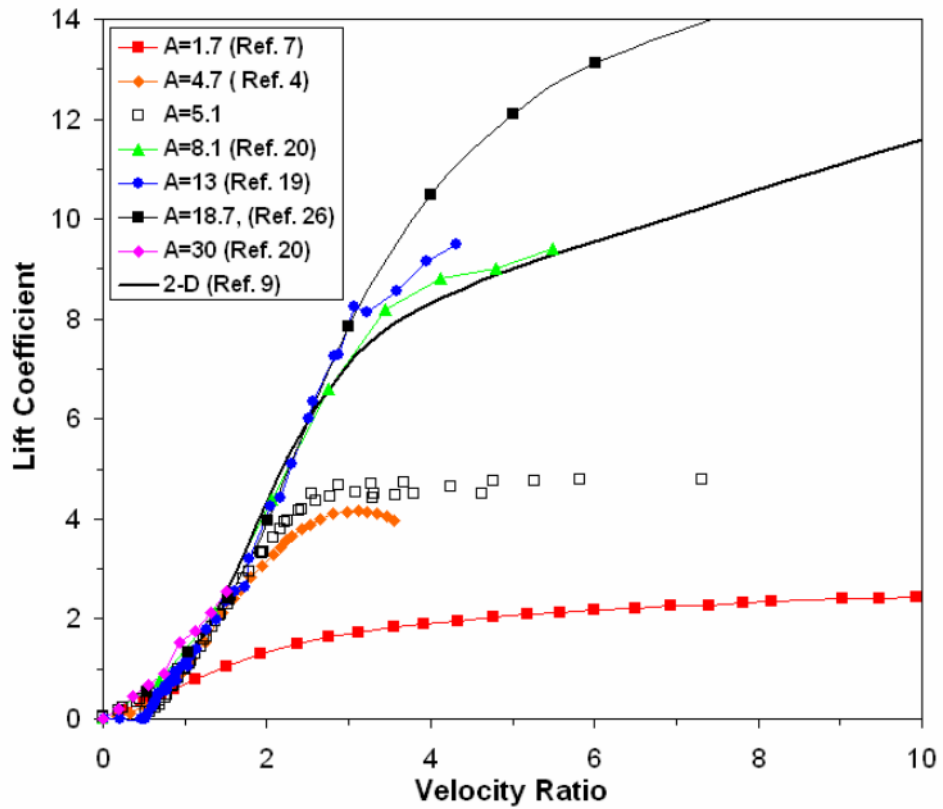


Figure 2.10: (a) Experimentally determined Magnus coefficients of rotating cylinders of varied rotation numbers \mathbf{R} and aspect ratios AR as summarized by Badalamenti. A generally-consistent trend in C_M with \mathbf{R} and AR is apparent. Credit: Badalamenti [2].

The aspect ratio of *R. ciliatiflora* seeds is on the order of 0.1, much smaller than those reported by Badalamenti. As such, we rely on experimental measurements of flying *R. ciliatiflora* seeds to determine approximate Magnus coefficients. The axial symmetry of the seeds of *R. ciliatiflora* means that the conventional lift experienced by seeds flying in a backspinning orientation is near zero; any force perpendicular to the freestream flow can be attributed to the Magnus effect. Video analysis conducted by Cooper [6], [7] yields a value for C_M of approximately 0.035. The component-wise representation of the Magnus force is given as

$$F_{Mx} = C_M \rho \frac{|\mathbf{V}|^2 \omega}{|\mathbf{L}|} (2rd)(L_y V_z - L_z V_y) \quad (2.39)$$

$$F_{My} = C_M \rho \frac{|\mathbf{V}|^2 \omega}{|\mathbf{L}|} (2rd)(L_z V_x - L_x V_z) \quad (2.40)$$

$$F_{Mz} = C_M \rho \frac{|\mathbf{V}|^2 \omega}{|\mathbf{L}|} (2rd)(L_x V_y - L_y V_x) \quad (2.41)$$

2.5 Aerodynamic Torques

The lift force is the only force which does not act at the center of mass. It is most convenient to represent the lift acting at the aerodynamic center of the disc, which is the point at which the torque imparted by the lift does not vary as a function of α . Potential flow theory shows that, for a thin, symmetric airfoil, the aerodynamic center is located at the quarter-chord point, 25% behind the leading edge of the disc [1]. For a round disc, the average quarter-chord point is a distance of $\pi r/8$ from the center of the disc [16]. A force acting at this point would induce a torque in the direction that increases α

$$|\tau_{lift}| = \left(\frac{\pi r}{8}\right) \left(\frac{\pi^2 r^2}{2} \rho |\mathbf{V}|^2 \sin(2\alpha)\right) \sin(\theta) = \frac{\pi^3 r^3}{16} \rho |\mathbf{V}|^2 \sin(2\alpha) \sin(\theta) \quad (2.42)$$

For a nonrotating disc, this torque would quickly align the disc perpendicularly to the flow. The spinning disc, however, instead precesses about the velocity vector, much like gravity makes a spinning top precess about the vertical axis. The rate of this precession is given by

$$\frac{d\phi}{dt} = -\frac{|\tau_{lift}|}{|\mathbf{L}| \sin(\theta)} = -\frac{\pi^3 r^3 \rho |\mathbf{V}|^2}{16 |\mathbf{L}|} \sin(2\alpha) \quad (2.43)$$

Cooper used a similar approach to characterize the disc's precession and show that it stabilizes it in a low drag configuration [7], which increases seed launch range as compared to a nonrotating or spherical seed.

The precession of the disc does not impact the angle of attack α . However, all forces influence the velocity \mathbf{V} of the disc, which can impact α depending on the force direction. The drag force only impacts the magnitude of \mathbf{V} , leaving α unaffected. In a similar vein, while the Magnus force does impact the direction of \mathbf{V} , it acts perpendicularly to both \mathbf{L} and \mathbf{V} , so it does not impact the angle of attack. The lift force acts to bring velocity in line with the chord of the disc, decreasing α . In contrast, a component of the gravitational force acts in the opposite direction, increasing α . Combining the effects of lift and weight yields the following expression for the rate of change of α

$$\frac{d\alpha}{dt} = g \frac{\sqrt{V_x^2 + V_z^2}}{|\mathbf{V}|^2} \cos(\phi) - \frac{\rho |\mathbf{V}| \pi^2 r^2}{2m} \sin(2\alpha) \quad (2.44)$$

It is important to note that this effect is not due to physical torques. It is purely the result of defining the body frame with respect to the disc's velocity vector, which changes over the course of flight.

2.6 Equation of Motion

Using the results of the previous sections, we can construct the equation of motion for the thin spinning disc. From Section 2.5, we take the expressions for α and ϕ , equations (2.44) and (2.43), respectively. From Section 2.4, we combine the component-wise expressions for \mathbf{F}_D , \mathbf{F}_L and \mathbf{F}_M (equations (2.26) through (2.28), (2.35) through (2.37), and (2.39) through (2.41), respectively) to obtain the forces acting on the disc in each of the laboratory frame directions. All told, the resulting equation of motion is a system of 5 coupled nonlinear differential equations, given below

$$\dot{\alpha} = g \frac{\sqrt{V_x^2 + V_z^2}}{|\mathbf{V}|^2} \cos(\phi) - \frac{\rho |\mathbf{V}| \pi^2 r^2}{2m} \sin(2\alpha) \quad (2.45)$$

$$\dot{\phi} = -\frac{\pi^3 r^3 \rho |\mathbf{V}|^2}{16 |\mathbf{L}|} \sin(2\alpha) \quad (2.46)$$

$$\ddot{x} = \frac{1}{m} (F_{Lx} + F_{Mx} - F_{Dx}) \quad (2.47)$$

$$\ddot{y} = \frac{1}{m}(F_{Ly} + F_{My} - F_{Dy} - mg) \quad (2.48)$$

$$\ddot{z} = \frac{1}{m}(F_{Lz} + F_{Mz} - F_{Dz}) \quad (2.49)$$

This set of equations describes the motion of a thin, spinning disc as it flies through a fluid medium.

Chapter 3

MATERIALS & METHODS

3.1 Video Analysis & Coefficient Extraction

As mentioned in the previous chapters, the Magnus coefficient C_M of a spinning cylinder is a function of several variables; the rotation number $\mathbf{R} = \frac{\omega r}{|\mathbf{V}|}$, the aspect ratio $AR = \frac{d}{r}$, and cylinder surface roughness. Since values of C_M in the parameter space occupied by *Ruellia ciliatiflora* have not yet been measured in wind tunnel tests, they must be determined experimentally through analysis of recorded seed flights. We can also use this method to determine the drag coefficient of *R. ciliatiflora* seeds more accurately than the flat plate value of $C_D = 1.28$. Cooper recorded and analyzed dozens of seeds of *R. ciliatiflora* and other similar ballochores; the following discussion results directly from his work.

Experimental setup

Cooper recorded the flight trajectories of *R. ciliatiflora* seeds using a Vision Research Microchrome high speed camera recording between 2000-3000 fps. Given the disparity between seed size (order 1mm) and dispersal range (order 10m), Cooper chose to record close up videos of seed dispersal events, capturing high-resolution video of the first 1m of the seeds' flight at the cost of missing the remaining portion of the flight. For our purposes of extracting aerodynamic coefficients from video analysis, this choice yields video of sufficient resolution to accurately measure the aerodynamic effects.

Video Analysis & Coefficient Extraction

Cooper wrote MATLAB scripts that tracked the locations of the seeds in the video frame, which can be used to calculate the aerodynamic forces experienced by the seeds. The changes in seed velocity can be used to determine the net acceleration of the seed, which can then be broken into components corresponding to accelerations due to gravity, lift, and drag. Gravity always acts in the negative y direction with magnitude $g = 9.81 \frac{m}{s^2}$. This constant acceleration can be subtracted from the net acceleration measured via video frame analysis to isolate the effects of aerodynamic forces. The net aerodynamic acceleration can be further subcategorized into two components, one parallel to the seed's velocity and one perpendicular. For a

rotationally-symmetric disc flying close to a backspin orientation, at a rotation rate of 0 the airflow over the top and bottom surfaces of the disc will be of equal velocity. Therefore, by Bernouli's principle, the pressures on the two surfaces of the disc will be equal, meaning that "conventional" lift is effectively 0. As such, any acceleration in the perpendicular direction calculated via video frame analysis is attributable to the Magnus effect. A ballistic Magnus parameter $k_M = \frac{a_{\perp}}{|\mathbf{V}|^2}$ of dimension $\frac{1}{m}$ can be computed from the video frame analysis. The Magnus force is proportional to the ballistic Magnus parameter

$$|\mathbf{F}_M| = m k_M |\mathbf{V}|^2 \quad (3.1)$$

The seed can be weighed after flight to determine the mass m and measured to yield its area A . Then, a numeric value for $|\mathbf{F}_M|$ can be calculated. Rewriting the original definition of the Magnus force in equation (2.38), we can extract the dimensionless Magnus coefficient C_M with

$$C_M = \frac{|\mathbf{F}_M|}{\frac{1}{2} \rho |\mathbf{V}|^2 A} \quad (3.2)$$

From Cooper's analyses, we find that the average C_M for *R. ciliatiflora* seeds is 0.035. We can conduct the same analysis for the drag force acting antiparallel to the disc's velocity. A ballistic drag parameter $k_D = \frac{a_{\parallel}}{|\mathbf{V}|^2}$ of dimension $\frac{1}{m}$ can be computed from the video frame analysis. The drag force is then proportional to this ballistic drag parameter

$$|\mathbf{F}_D| = m k_D |\mathbf{V}|^2 \quad (3.3)$$

Using the seed's mass and area, we calculate the dimensionless drag coefficient C_D in the same manner as we calculated C_M

$$C_D = \frac{|\mathbf{F}_D|}{\frac{1}{2} \rho |\mathbf{V}|^2 A} \quad (3.4)$$

Cooper's data reveals an average drag coefficient C_D of 0.301, an order of magnitude larger than the Magnus coefficient. It should be noted this experimental drag coefficient does not account for lift-induced drag; we must still add the additional induced drag component $\frac{\pi^2 \sin(\alpha)^2}{e}$ to C_D . While the theoretically-derived

expressions for C_M and C_D allow for the broad application of the derived equation of motion to any part of parameter space, since our ultimate motivation is to study the dispersal of *R. ciliatiflora* seeds, we substitute these experimentally-determined expressions into the equation to maximize its accuracy in simulating the trajectories of the seeds in question, replacing the previously .

3.2 Numerical Trajectory Simulation

At this point, we are ready to implement the derived equation of motion into *Wolfram Mathematica*, a technical computing package in which it is easy to numerically solve differential equations and visualize the results. The *Mathematica* function `NDSolve` is a numerical solver capable of calculating approximate solutions to a wide range of differential equations. Many *Mathematica* functions are black boxes in which it is not immediately apparent to the user how the function actually operates. From the documentation for *Mathematica*'s `NDSolve` function [13]

`NDSolve` has many methods for solving equations, but essentially all of them at some level work by taking a sequence of steps in the independent variable x , and using an adaptive procedure to determine the size of these steps. In general, if the solution appears to be varying rapidly in a particular region, then `NDSolve` will reduce the step size or change the method so as to be able to track the solution better.

For the purposes of this thesis, so long as the calculated solutions to the equation of motion appear reasonable, the exact method by which they were calculated is unimportant. The approximations used to simplify the representation of the aerodynamic forces acting on the flying disc, as compared to a true CFD simulation in which the forces are calculated directly from the governing Navier-Stokes equations, lead to a (comparatively) simpler equation of motion that is unlikely to be subject to numerical stability issues. As such, the choice of numerical method employed to calculate solutions is of little concern. As will be shown in the following chapter, numerical instabilities are uncommon, only occurring at extreme values of the initial conditions far from regions of interest. For further reading on the intricacies of *Mathematica*'s `NDSolve` function, consult [12].

The *Mathematica* scripts that were used in this thesis are available https://github.com/hessewithbroej/Ugrad_disc_thesis. In the following sections, we outline the structures and purposes of these scripts.

Implementing Equation of Motion in *Wolfram Mathematica*

The first script constructed for use in this thesis is *full5_drag_lift_g.m*. This script implements and solves the equation of motion for a given set of initial conditions. Using the generated solution, the script creates several visuals of the disc's trajectory and orientation, and the forces experienced by the disc, over the course of the flight for use in ensuring all the terms of the equation are behaving as they should. Finally, the script contains an animation of the seed's trajectory and orientation as it flies.

The first block of code is a simple constants definition. It is here where the various physical constants like the density of air and disc parameters like radius and spin rate are inputted. These are used in the following block to calculate the forces experienced by the disc.

The second block of code contains the implementations of the three components of the aerodynamic forces as expressed in the laboratory frame. The magnitudes of each of the three forces, lift, drag, and the Magnus force, in each of the three directions of the laboratory frame are expressed as a function of flight parameters, which vary with time. Each component of each force is stored in a variable for later use. While not strictly necessary, this block allows us to separate the force definitions from the equation of motion definitions, improving readability and debugging. As written, these equations utilize experimentally-measured aerodynamic coefficients that are only valid for seeds of *R. ciliatiflora*; to simulate other seeds or discs, these coefficients will likely need to be changed.

The third block contains the five equations that combine to form the overall equation of motion for the flying disc. The equations are expressed in terms of the component-wise force definitions resulting from the previous block.

In the fourth block, all the initial conditions necessary to solve the equation of motion are defined and the solution is computed. Since this block is where the numerical solving actually takes place, it is the most computationally demanding, but since the flight of the discs is generally short (around 1 s), the solutions do not usually take long to generate. The user must specify the length of the flight to simulate. An arbitrary value of 10 seconds was chosen but may need to be increased if other discs outside the realm of *R. ciliatiflora* seeds are to be simulated. For numerical stability purposes, it is generally best for the initial launch angles α and ϕ to be very slightly perturbed slightly from round multiples of $\frac{\pi}{2}$. The constraint on the lift direction that dictates it act in the plane defined by \mathbf{L} and \mathbf{V} can lead to an

underconstrained system in certain orientations. Certain combinations of α and ϕ lead to colinear arrangements of \mathbf{L} and \mathbf{V} . When colinear, these vectors do not define a unique plane and therefore the lift force is not uniquely specified. Physically, these orientations all correspond to symmetric cases where the lift would be 0, but the numerical solver is incapable of handling these scenarios. While these cases should never be reached by the solver, adding a small displacement ϵ to the initial angles will ensure these cases are avoided without impacting the results.

The fifth block uses the results of the numerical solver to generate visualizations of the disc's flight trajectory. The magnitudes of the aerodynamic forces in each of the dimensions of the laboratory frame are plotted as a function of time, facilitating comparisons between the different forces influencing the flight of the disc. The body frame angles α and ϕ over the course of the flight are also plotted.

The final block animates the disc's dynamics over the course of the flight. The orientation and trajectory of the disc with respect to the laboratory frame is visualized. Additionally, vectors representing the forces impacting the discs are included, varying in direction and magnitude over the course of the flight.

Functional Batch Simulator

The second script constructed for this thesis is titled *Functional_solver.m*. It takes the implementation of the equation of motion from the previous script and creates a batch processing function that allows for the simulation of a large number of initial condition sets. The script also generates contour plots of the results of these simulations, aiding in the visualization of how different initial launch conditions co-vary to influence launch range.

As with the previous script, the first block of the second script contains simple constants definitions. The second block contains a custom function named `solveEquations`. The arguments to `solveEquations` are the initial conditions to be used in solving the equation of motion. `solveEquations` uses the constants defined in the first block in conjunction with user-provided initial conditions arguments to define expressions of the aerodynamic forces in the three directions of the laboratory frame, and to define and solve the equation of motion. Essentially, this block merges blocks 2, 3, and 4 of the previous script into a single function that facilitates the simulation of large numbers of flights under a range of initial conditions. The function outputs a list of the following simulation parameters: $\{\phi_o, \alpha_o, \beta_o, \omega, \text{flight time}, \text{net horizontal displacement}, \text{and off-horizontal displacement}\}$.

The remainder of the blocks use *Mathematica*'s `Table` function to call `solveEquations` a number of times with varying sets of initial conditions and visualize the results. The `Table` function is similar to a for-loop in a more conventional programming language; it runs a function a specified number of times with varying inputs, storing the results of said calculations in a `list` object. The first argument of `Table` is the function to be executed. The remaining arguments are the variables to be iterated and passed into a function, each represented using a `list` object with the variable and a sub-list containing the values of that variable to pass to the function. Any number of variables may be included in the `Table` call, with each additional variable acting like a nested for-loop; two variables in a `Table` call is equivalent to a double nested for-loop and the results are given as a two-dimensional list; three variables equivalent to a triple nested for loop with results given in a three-dimensional list, and so on. As an example, the line

```
Table[solveEquations[ $\phi_o$ ], { $\phi_o$ , {0,  $\frac{\pi}{2}$ ,  $\pi$ ,  $\frac{3\pi}{2}$ }}]
```

would call the function `solveEquations` four times, one for each listed value of ϕ_o , and output the results of the function calls as a `list` of length 4.

C h a p t e r ~ 4

RESULTS & ANALYSIS

The following chapter details the results of simulating the flight of *R. ciliatiflora* seeds under a range of initial conditions, comparing the results of the simulations against launch parameters observed in nature.

4.1 Exploratory Simulation & Analysis

This section explores in detail the results of a handful of representative simulations in order to provide some intuition for later multivariate analyses. To provide a connection to everyday experience, we first simulate the flight of a drink coaster. The next time the reader finds themselves in a bar with some open space, they are encouraged to throw a couple coasters with a variety of initial orientations in order to gain some physical intuition for the flight of spinning discs. The parameters used in the simulation of coaster flight are given in Table 4.1 below.

Parameter	Description	Value
g	Gravitational Acceleration	9.81 m / s ²
ρ	Density of Air	1.225 kg / m ³
C_D	Drag Coefficient	1.28
C_M	Magnus Coefficient	.035
R	Coaster Radius	5.3 cm
d	Coaster Thickness	1.7 mm
m	Coaster Mass	5.9 g
β	Launch Angle	40 deg
ω	Spin Rate	7 Hz
$ \mathbf{V} $	Launch Velocity	10 m/s

Table 4.1: Numeric values of coaster launch parameters.

Backspinning Coaster

The simplest launch orientation is backspin. Cooper showed the backspin orientation is the only stable flight orientation; any other initial launch orientation will eventually converge to backspin [7]. We simulate the coaster flight from near-backspin using the launch parameters in Table 4.1 with an initial $\phi_o = 260^\circ$, slightly off of backspin, and an initial velocity that lies entirely in the vertical XY plane.

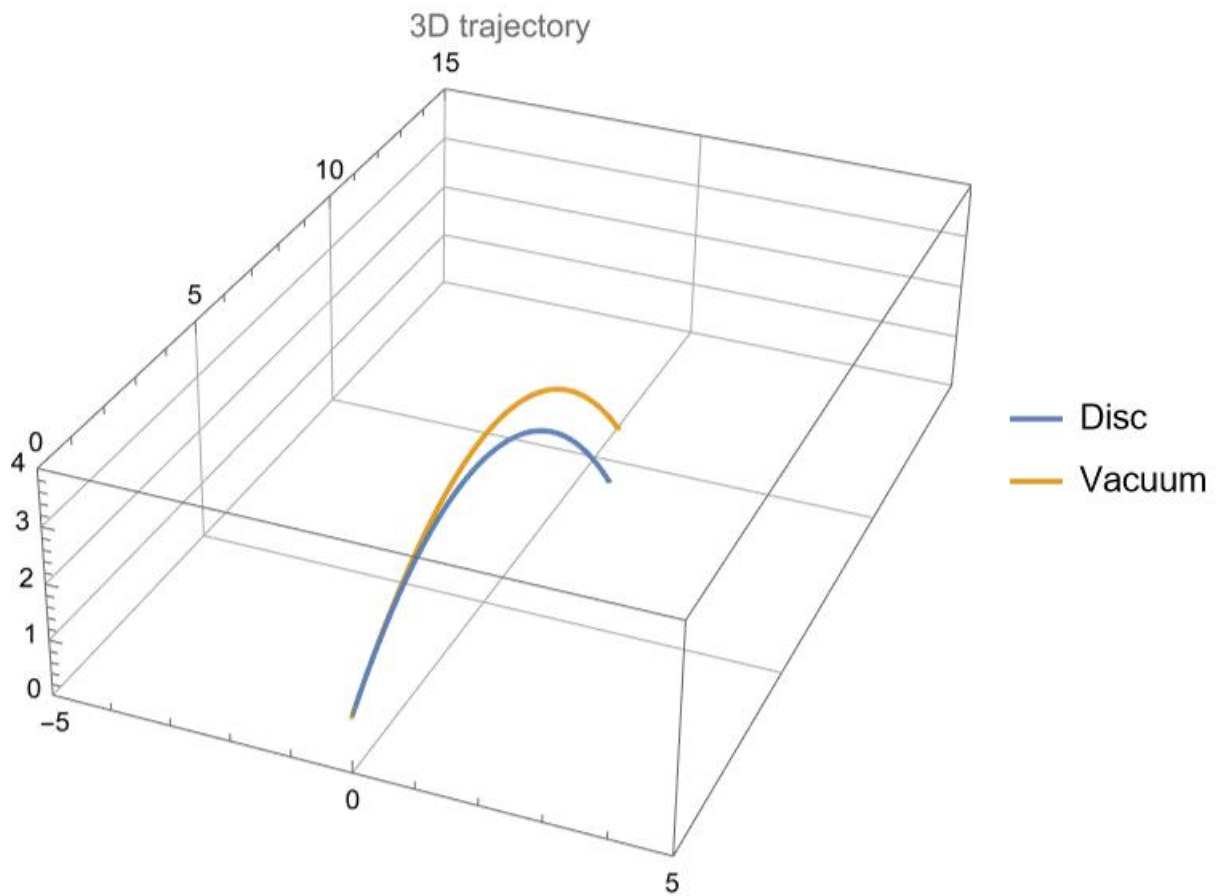


Figure 4.1: Three-dimensional view of backspinning coaster trajectory.

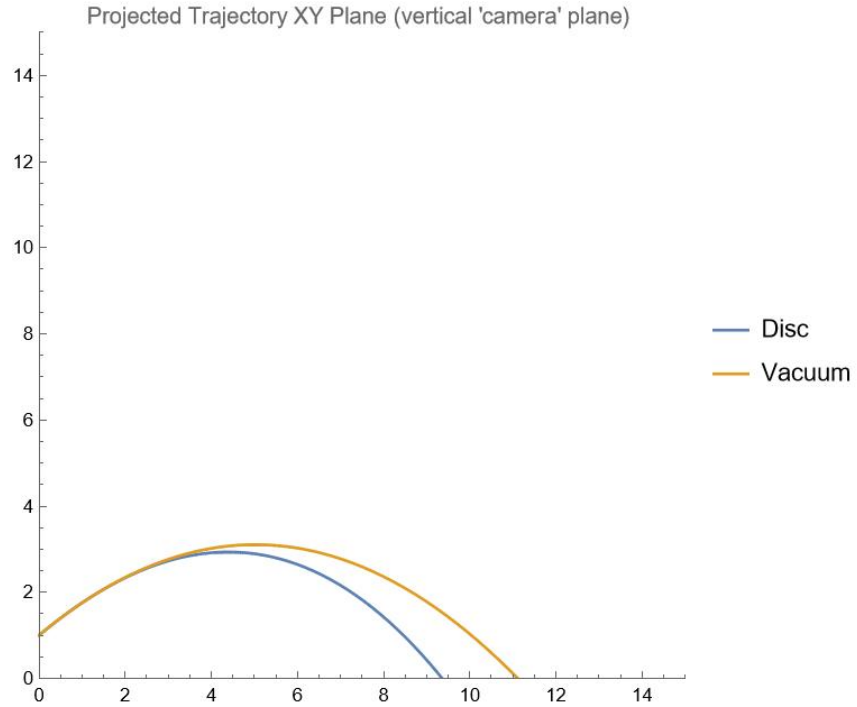


Figure 4.2: Side view of coaster trajectory when launched near backspin shows total range of approximately 10m.

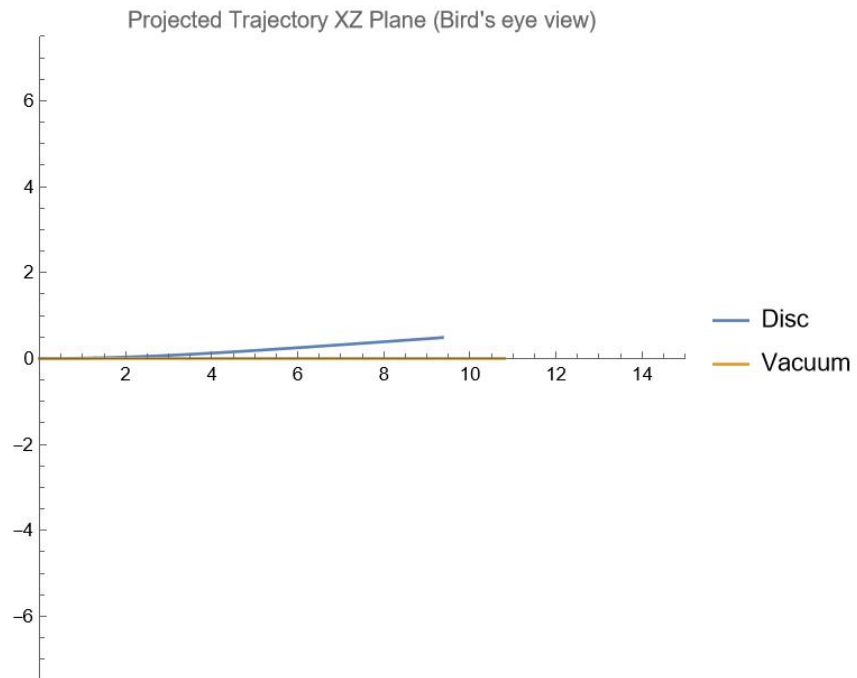


Figure 4.3: Bird's eye view of coaster trajectory when launched near backspin ($\phi = 260$) shows that off-horizontal displacement is minimal.

We see the trajectory of the backspinning coaster is not very different from an equivalent-mass particle launched in a vacuum. The slight off-horizontal displacement in the z direction seen in Figure 4.3 is the result of the slight perturbation to true backspin; if ϕ_o were 270° , there would be no off-horizontal displacement. These results qualitatively mesh with the observed flights of backspinning coasters.

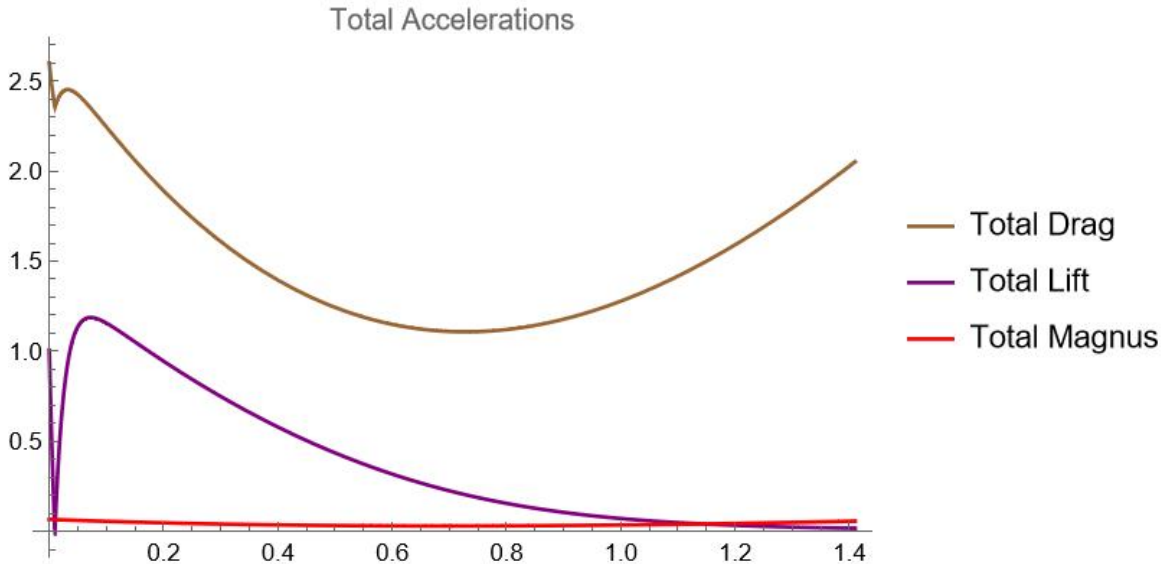


Figure 4.4: Aerodynamic accelerations experienced by coaster in backspin.

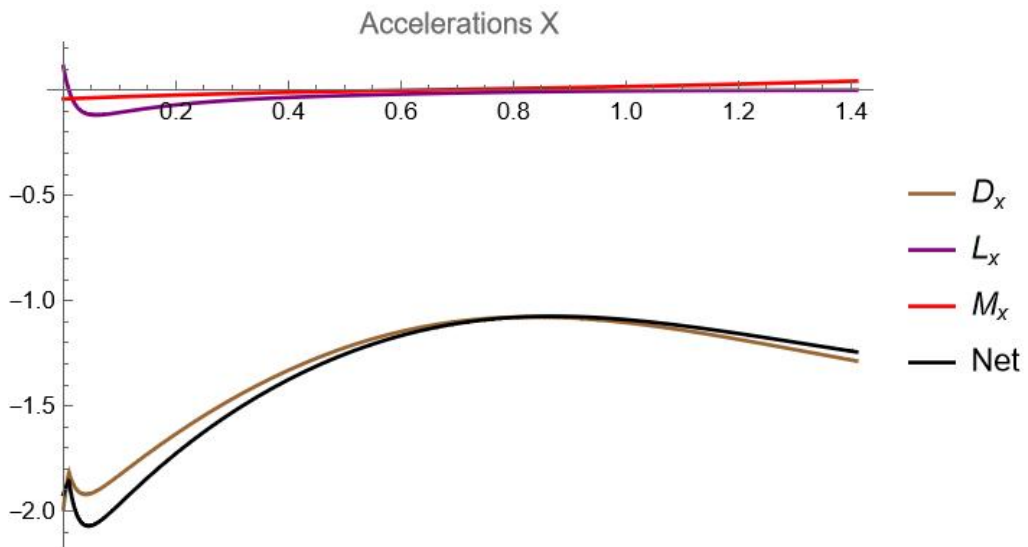


Figure 4.5: X components of aerodynamic accelerations in backspin. Drag strongly opposes the motion of the disc in the x direction, while the other forces are negligible.

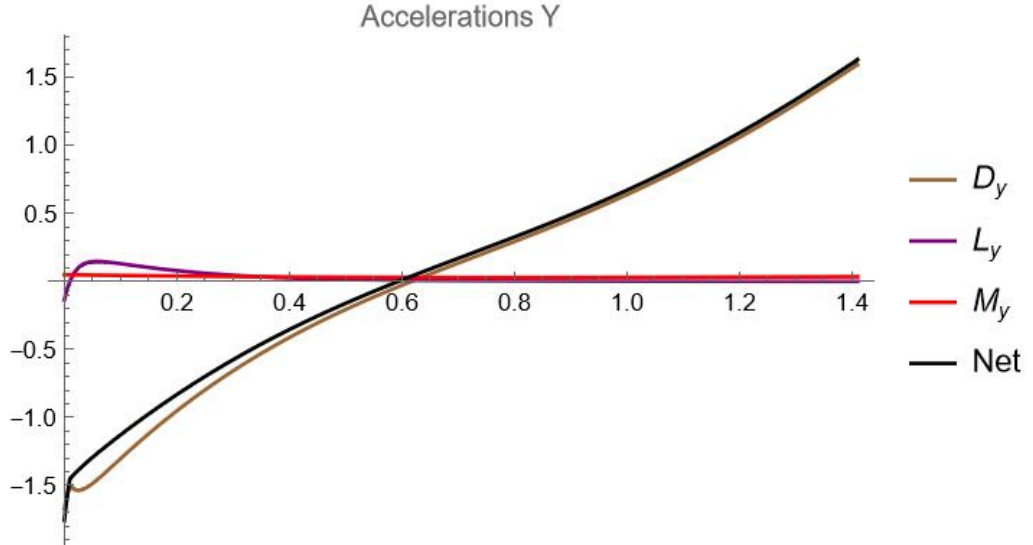


Figure 4.6: Y components of aerodynamic accelerations in backspin. The Magnus force is always directed upwards. After convergence to backspin, lift is 0.

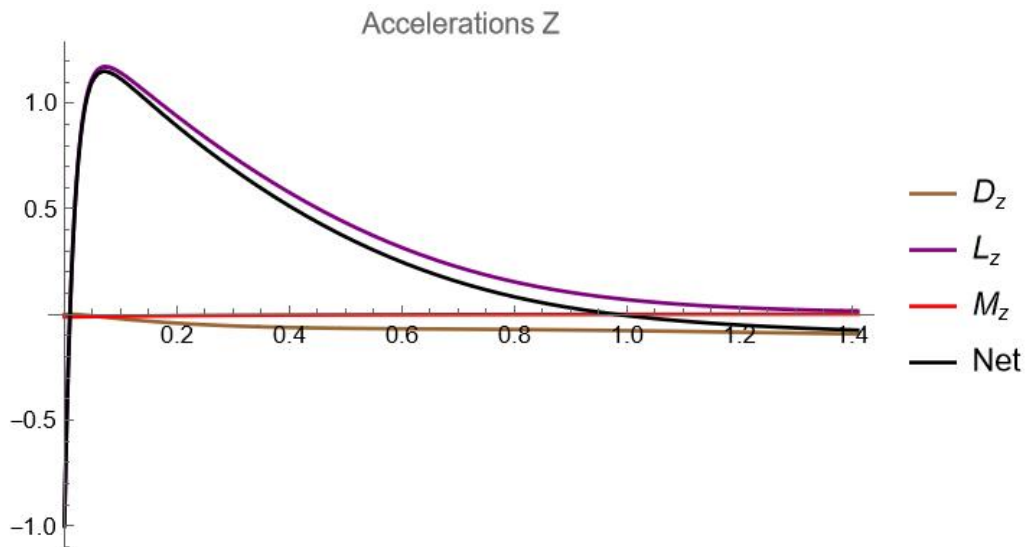


Figure 4.7: Z components of aerodynamic accelerations in backspin. The lift force is seen to be the force responsible for displacing the coaster in the z direction, while the other forces are negligible.

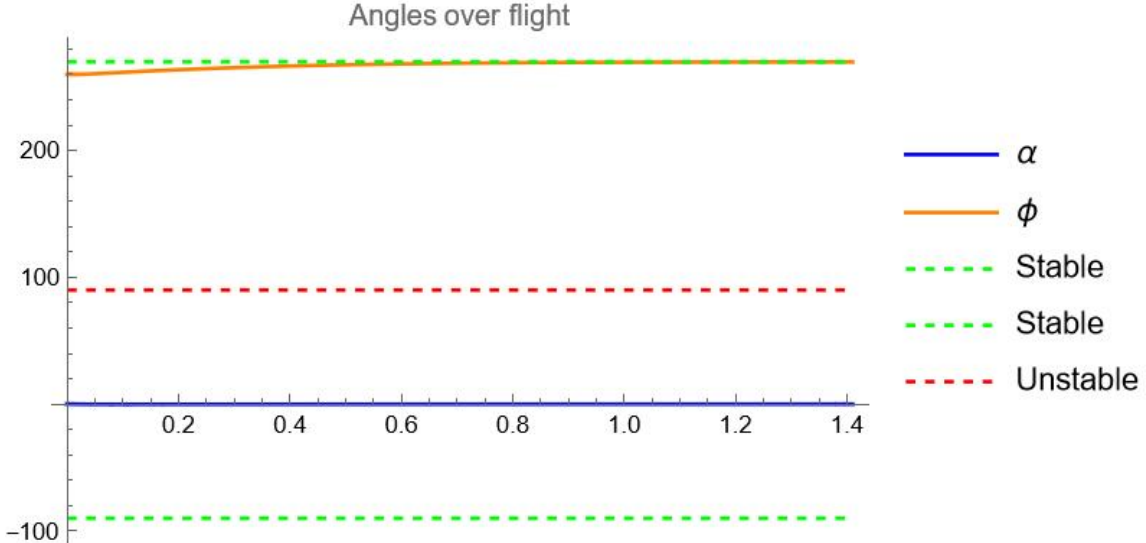


Figure 4.8: Angular dynamics over flight. ϕ quickly converges to backspin ($\phi = 270^\circ$), while α remains quite small over the course of the flight.

The angular dynamics of the coaster, plotted in Figure 4.8, show that ϕ converges to backspin and α remains small. Examining the accelerations experienced by the disc over the course of flight as plotted in Figure 4.4, we see drag is the dominant force acting on the backspinning coaster. Lift is appreciable in the portion of flight where the disc is not in perfect backspin, acting to displace the coaster in the z direction. As ϕ converges 270° , the lift is reduced to nearly 0. This is true in any of the orientations examined; lift is only a relevant force when the disc is out of the stable backspin orientation. Upon convergence to $\phi = 270^\circ$, lift is essentially nil.

Sidespinning Coaster

A sidespinning coaster is launched much like one would throw a Frisbee. There are two sidespin orientations, $\phi = 180^\circ$ rotates like a Frisbee thrown with a sidearm (also known as forearm or a flick), while $\phi = 0^\circ$ rotates like a Frisbee thrown with a backhand (the natural technique of most beginners). Here we simulate the disc flight using the conditions in Table 4.1 with $\phi = 180^\circ$

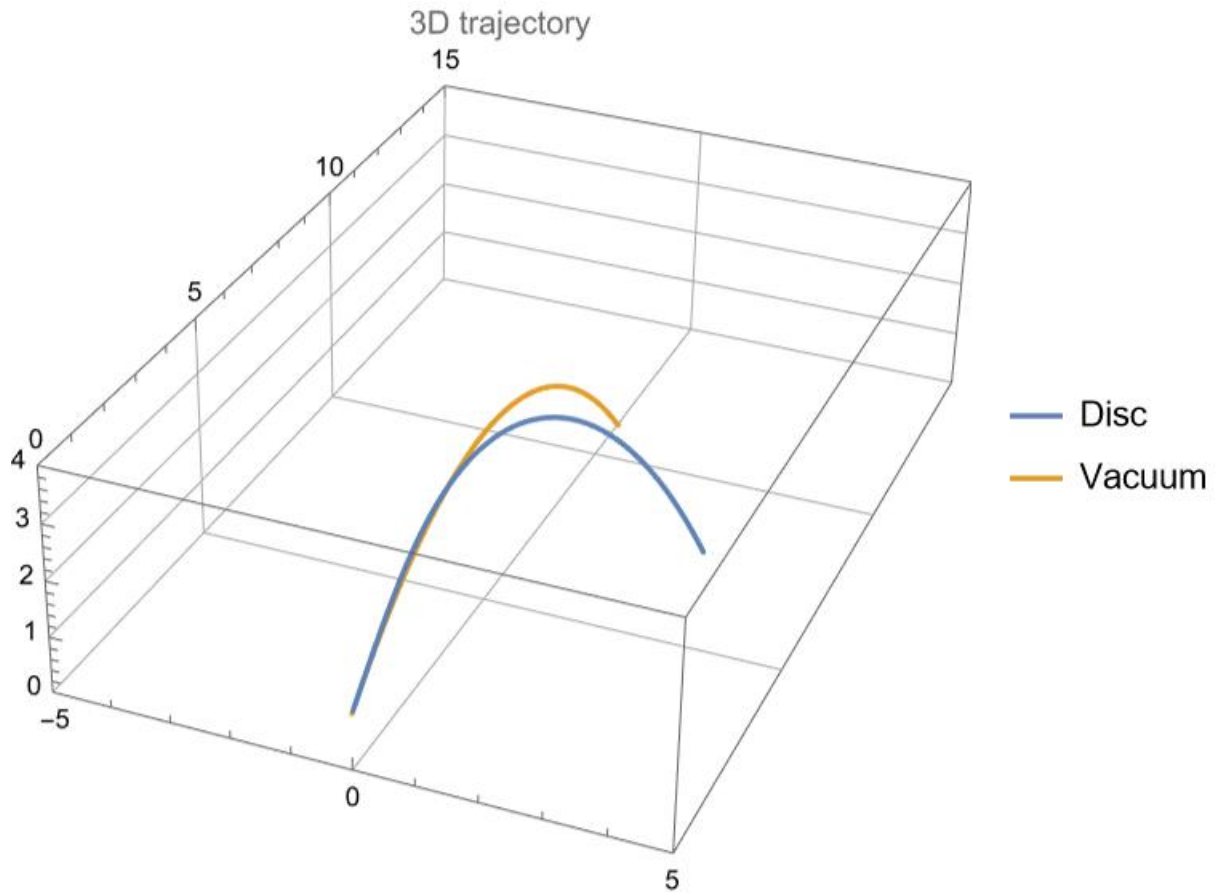


Figure 4.9: Three-dimensional view of sidespinning coaster trajectory.

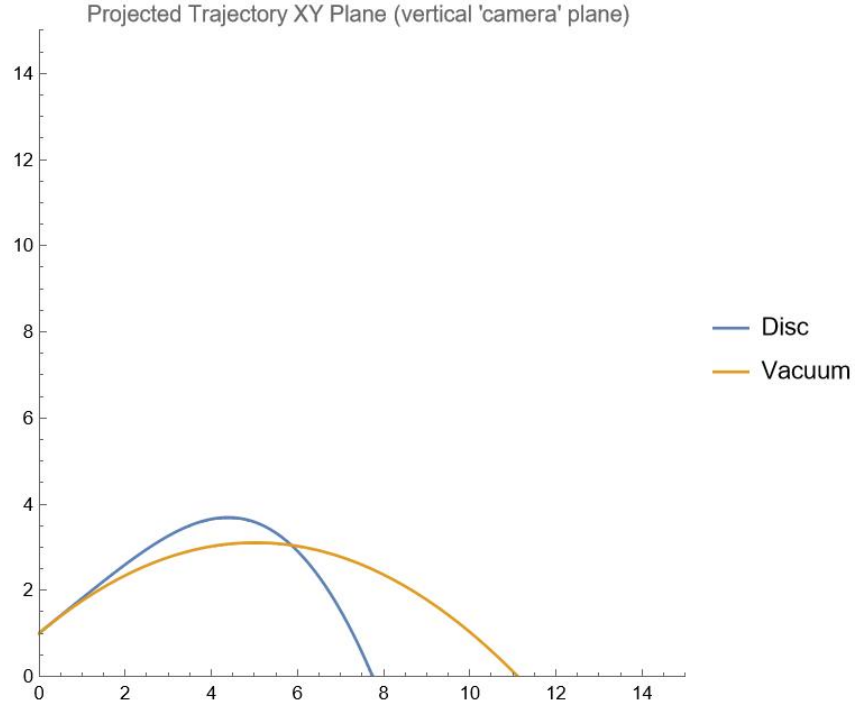


Figure 4.10: Side view of sidespinning coaster trajectory. Since the disc is initially oriented with a large planform area, the initial lift is of considerable magnitude. It acts in the positive y direction, pulling the disc above the trajectory that would be experienced by a particle in a vacuum.

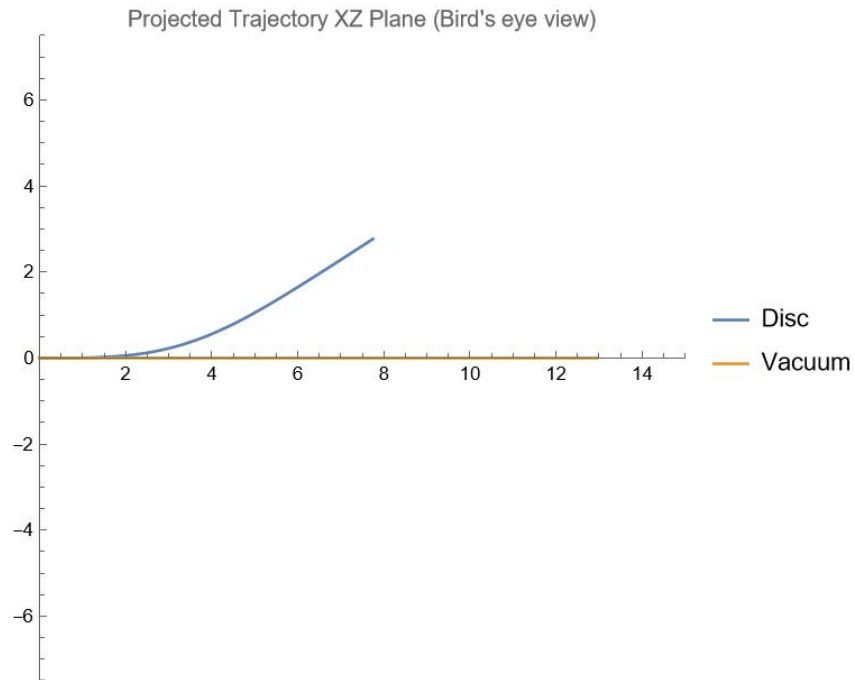


Figure 4.11: Bird's eye view of coaster trajectory when launched near sidespin shows an appreciable off-horizontal displacement of approximately 3m.

Starting far from backspin results in a larger off-horizontal displacement, as seen in Figures 4.9 and 4.11. The component-wise acceleration plots shown below reveal that the lift force is responsible for both keeping the disc aloft through a $+y$ acceleration and displacing the disc sideways through a $-z$ acceleration.

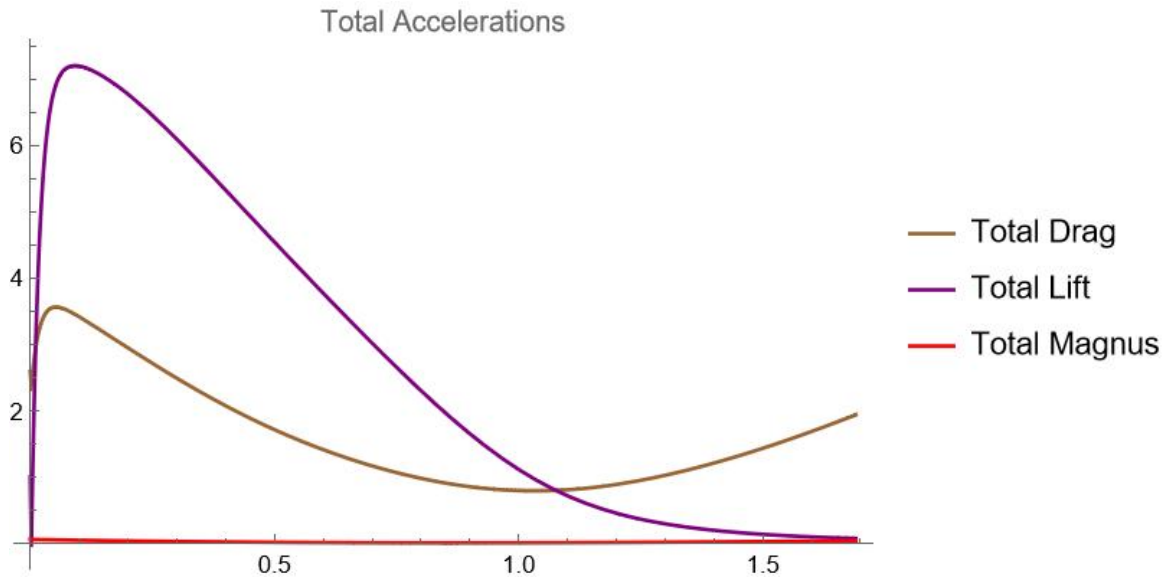


Figure 4.12: Aerodynamic accelerations experienced by coaster in sidespin.

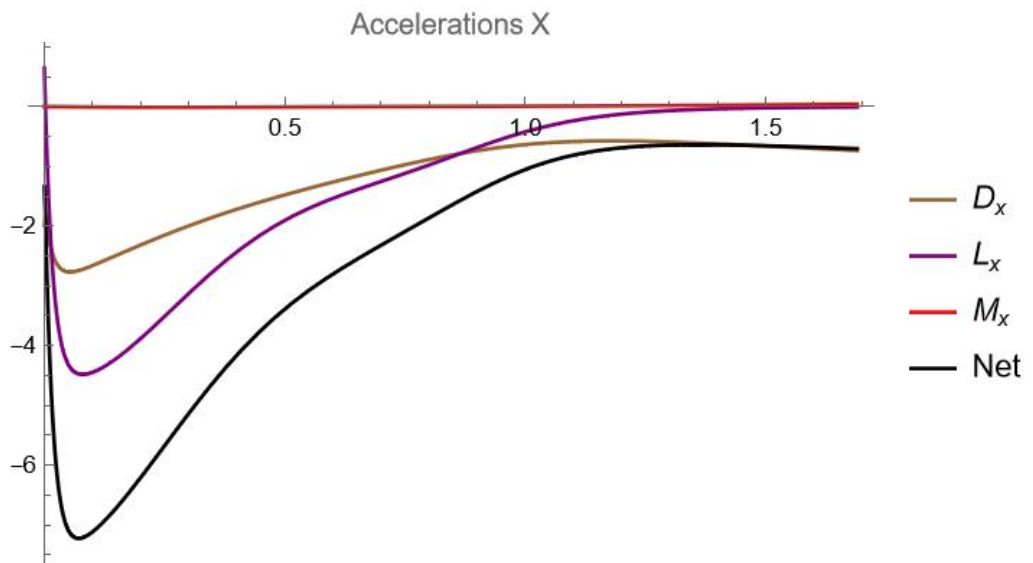


Figure 4.13: X components of aerodynamic accelerations in sidespin. Compared to the backspin case, lift in the x direction is significant.

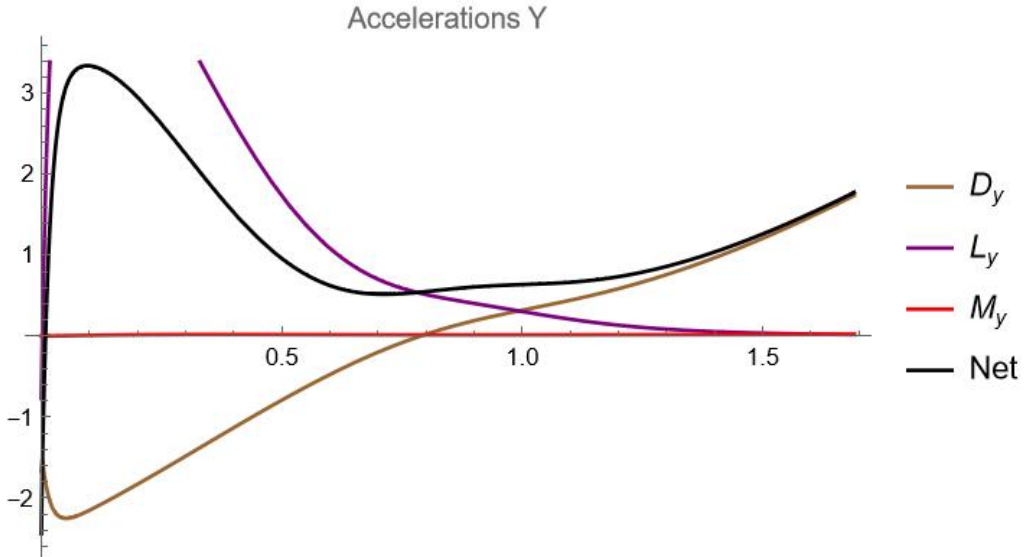


Figure 4.14: Y components of aerodynamic accelerations in sidespin. Lift is the force responsible for keeping the disc aloft longer than in the backspinning case.

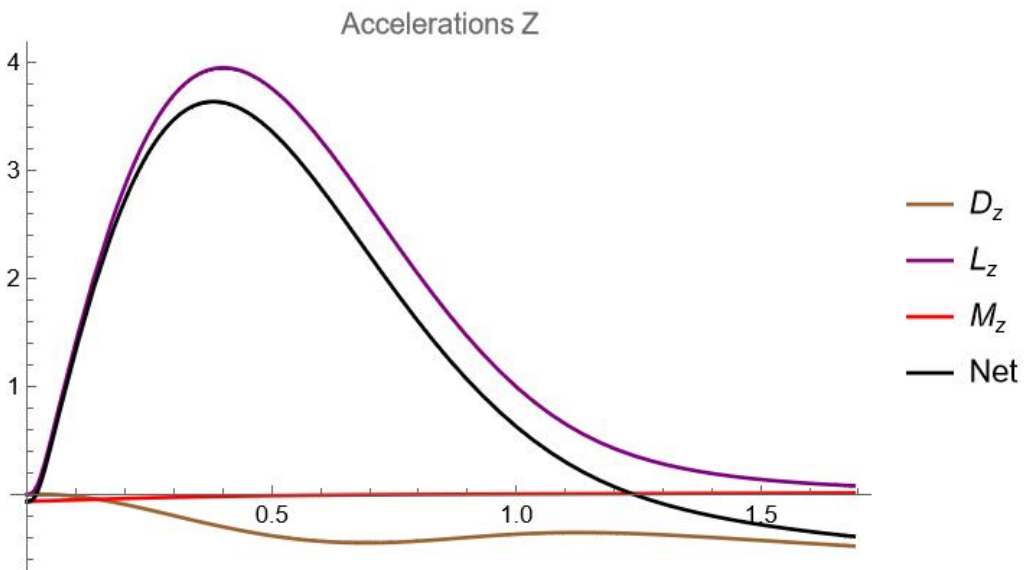


Figure 4.15: Z components of aerodynamic accelerations in sidespin. Lift is the force responsible for pulling the disc off of the original x direction of motion.

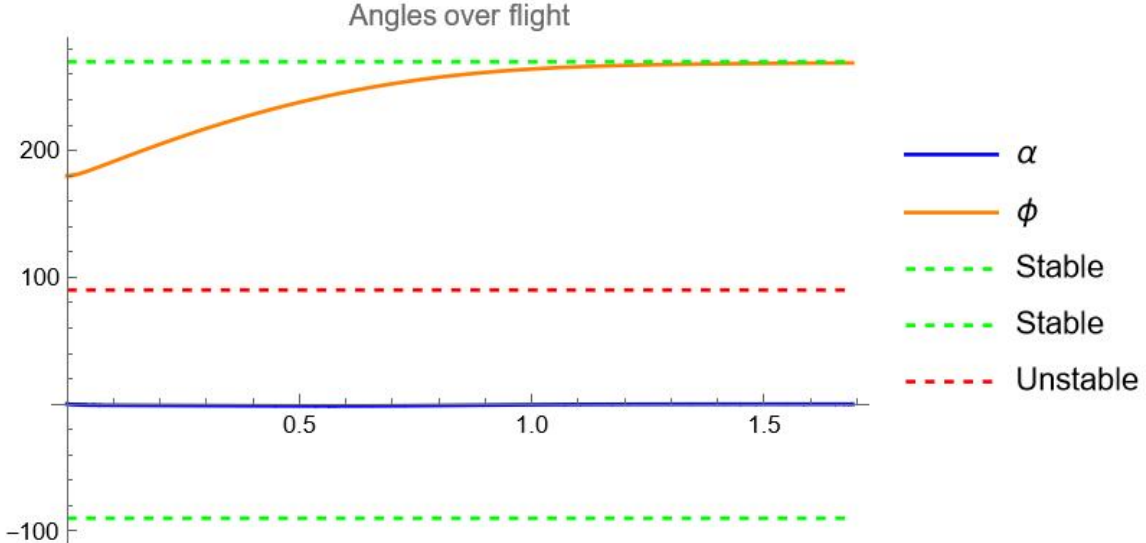


Figure 4.16: Angular dynamics over sidespin flight. ϕ converges to backspin on the order of 1 second, while α remains quite small over the course of the flight.

Topspinning Coaster

Topspin is the most interesting flight orientation due to its instability. Exact topspin at $\phi = 90$ is an unstable equilibrium that would act quite similarly to a flight in perfect backspin. Any real flight at topspin, however, will quickly be perturbed and converge to backspin. We simulate a near topspin flight using the parameters from Table 4.1 with $\phi_o = 100$.

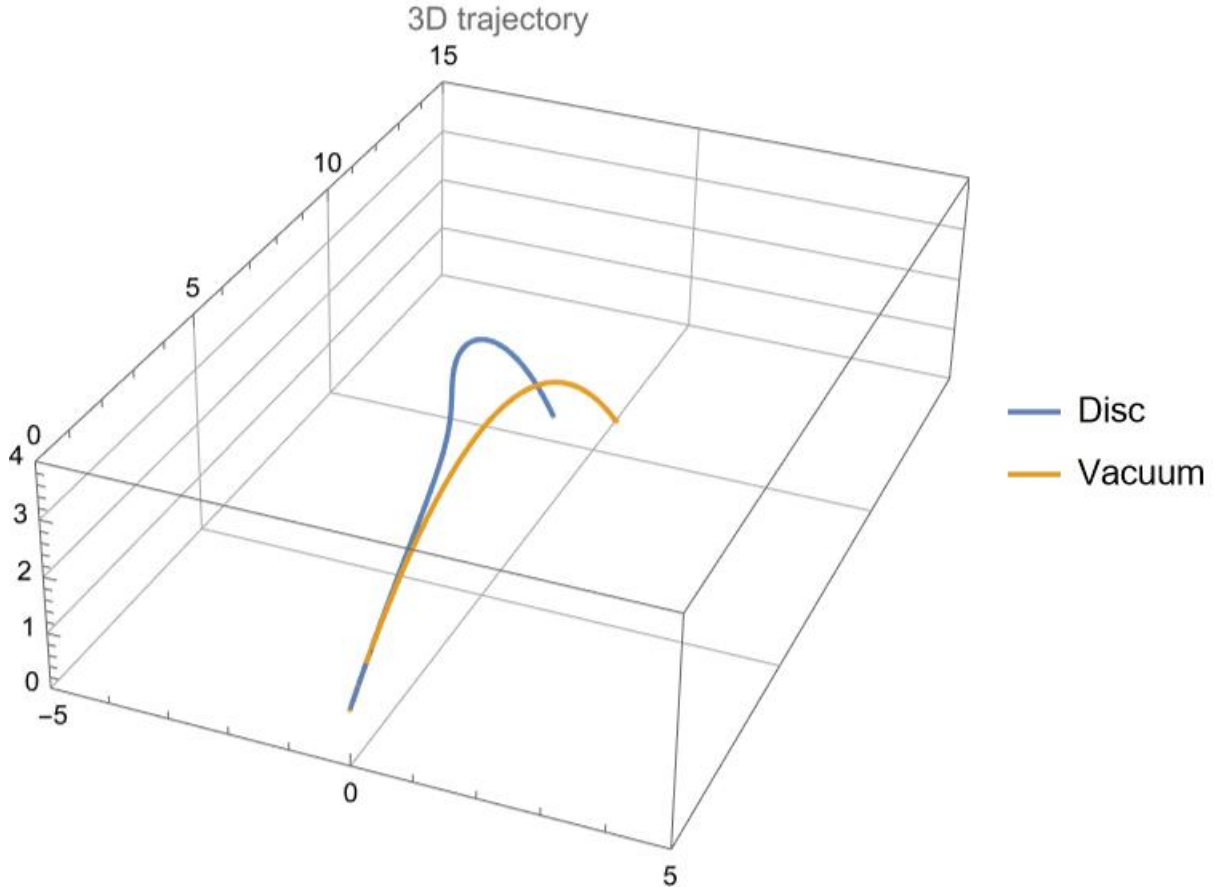


Figure 4.17: Three-dimensional view of topspinning coaster trajectory. Compared to a particle in a vacuum, the topspinning disc has an interesting trajectory, swinging outwards in the $-z$ direction at the apex of the flight before fading back inwards in the $+z$ direction. As the disc flips from topspin to sidespin, the lift force pulls the disc in the $-z$ direction. However, as the disc continues flipping from sidespin into backspin, the lift acts in the opposite direction, pulling the disc back in line with the initial trajectory.

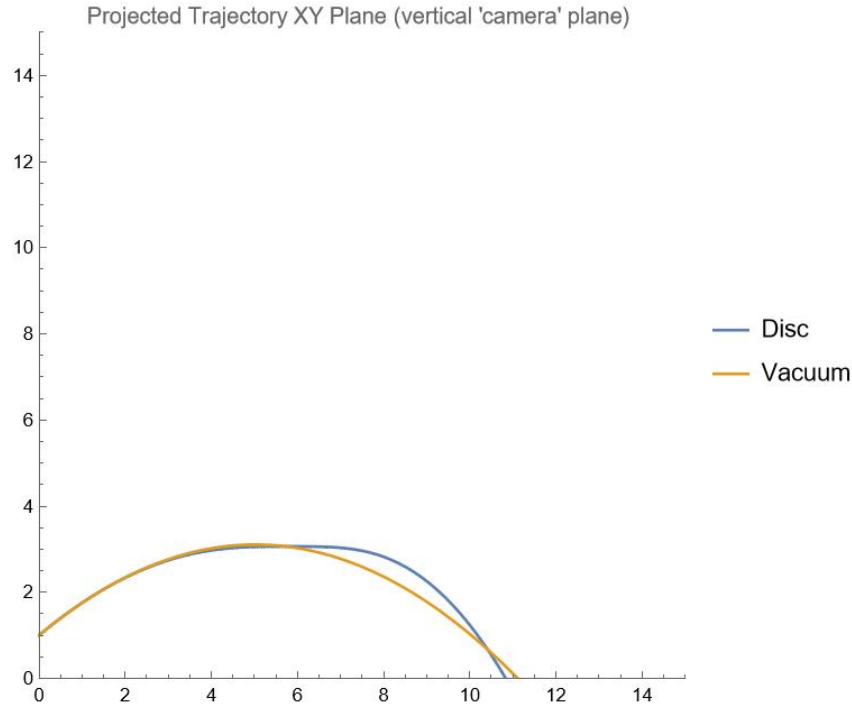


Figure 4.18: Side view of coaster trajectory when launched near topspin shows dispersal range is increased from the backspin orientation, rivaling that of an equivalent-mass particle in a vacuum.

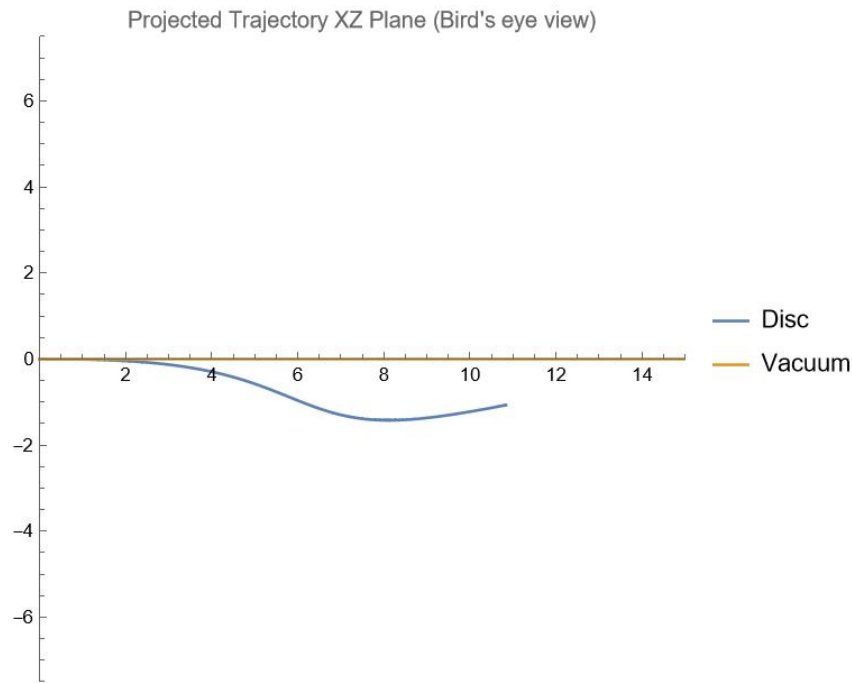


Figure 4.19: Bird's eye view of coaster trajectory when launched near topspin shows an off-horizontal displacement on the order of 1m.

As is apparent in Figures 4.18 and 4.19, the trajectory of the topspinning coaster is appreciably different from the backspinning one. The instability of the topspin orientation results in a "flipping" of the disc during flight, which in turn allows for more interesting aerodynamic forces.

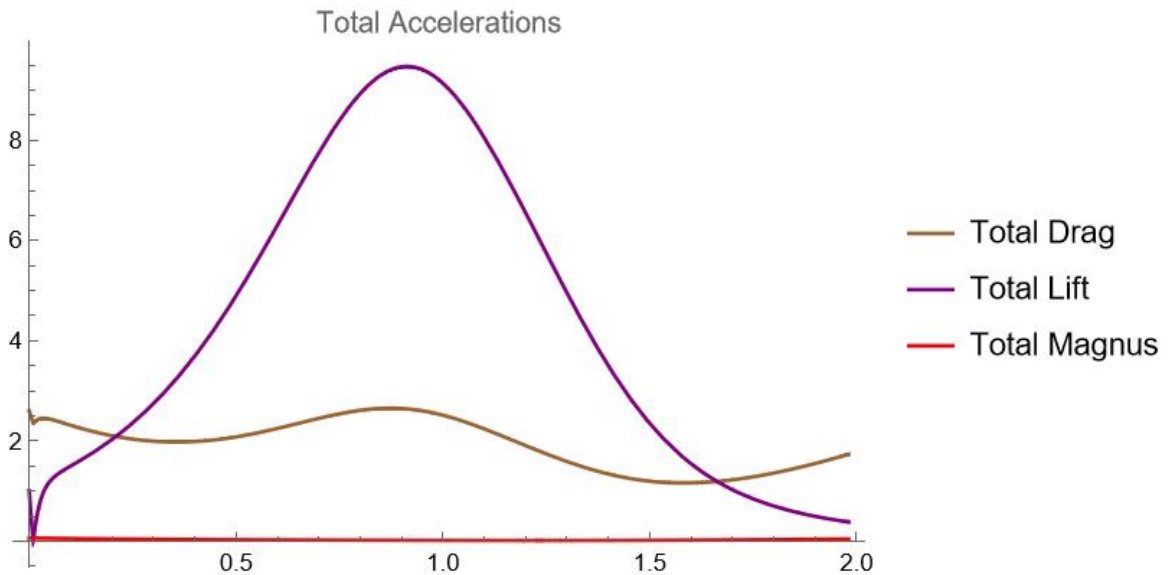


Figure 4.20: Net aerodynamic forces on the topspinning disc. Compared to the backspinning case, for the topspinning case, the lift force has an appreciable effect.

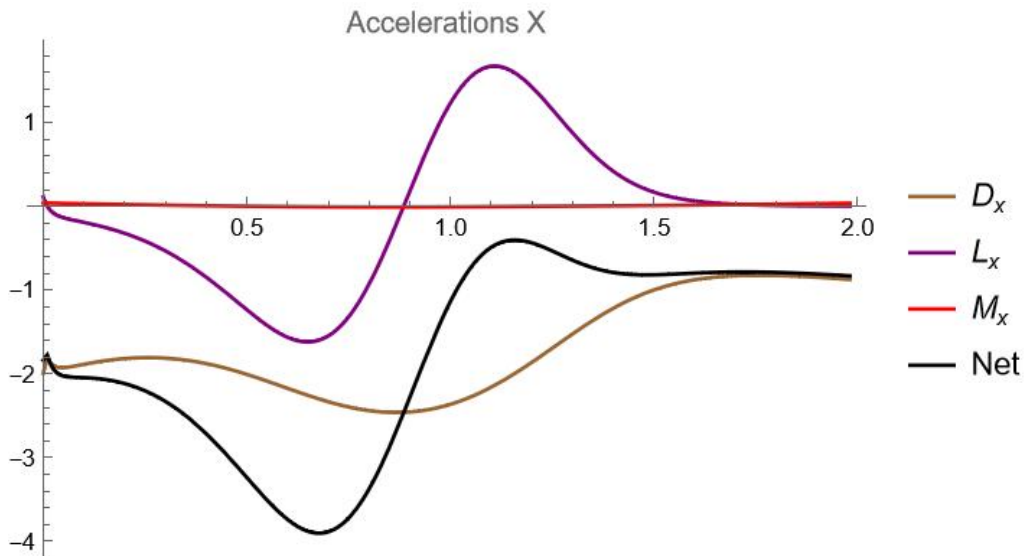
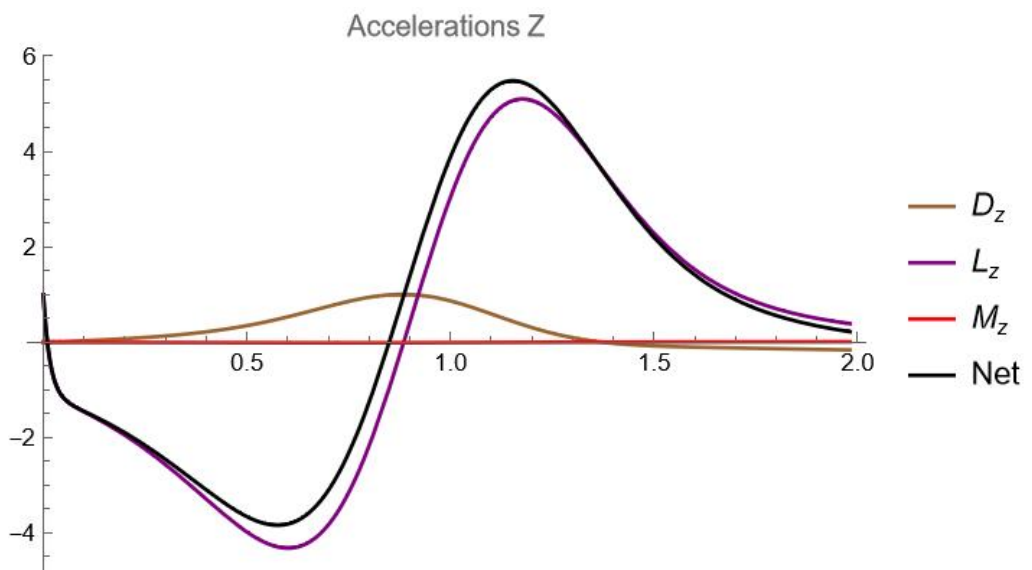
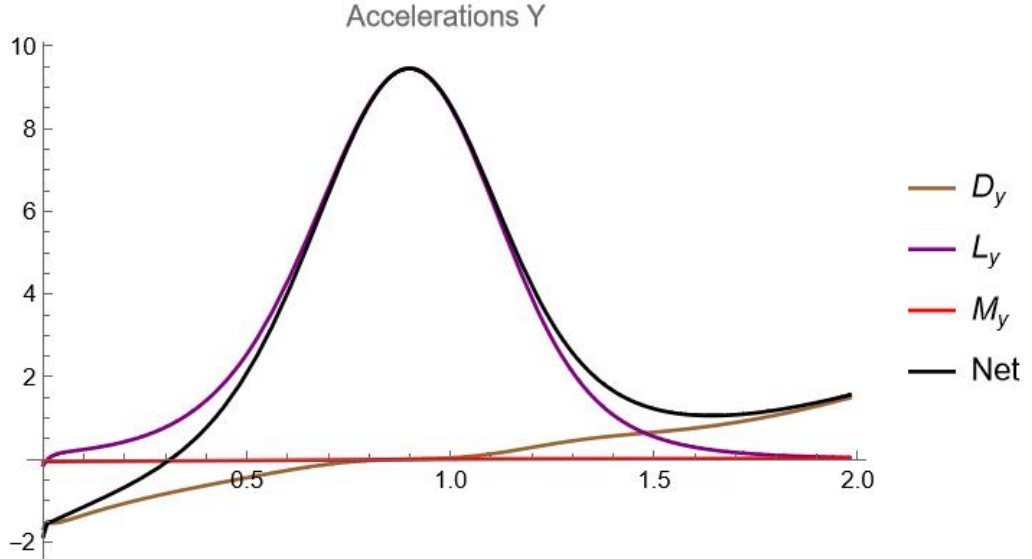


Figure 4.21: X components of aerodynamic accelerations. Drag strongly opposes the motion of the disc in the x direction. The lift force is roughly symmetric in the x direction, integrating the lift over time would show a small net contribution to x acceleration in the $-x$ direction.



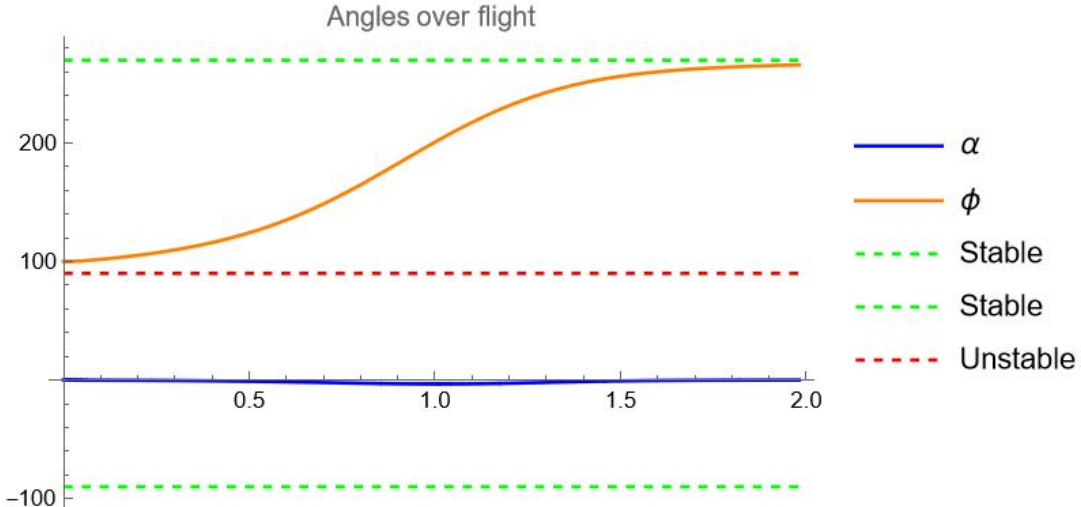


Figure 4.24: The angular dynamics of the topspinning coaster. We see the disc's orientation angle ϕ converges to the stable backspinning case on the order of 1.5 seconds.

As the coaster flips from topspin to backspin, it passes through the sidespin orientation in which planform area (projected area in the direction of the horizontal XZ plane) is maximized. In other words, the coaster's surface acts like a wing, generating lift in the positive y direction, which keeps the disc aloft longer than the backspinning case. This lift acts in both the negative and positive z directions in roughly equal magnitudes. Much of the off-horizontal z motion can therefore be attributed to the lift. Per Figure 4.23, the accelerations due to lift in the positive and negative z directions roughly cancel, leaving a small net displacement in the z direction at the end of the flight.

Summary of Coaster Flights

The results of simulating coaster flights at a variety of initial ϕ_o are given below in Table 4.2. The parameters used in the launch simulations are given in Table 4.1.

ϕ_o	Flight Time (s)	Range (m)	Z displacement (m)
90	1.43	10.66	0.31
100	2.05	13.81	-1.51
110	2.11	12.10	-0.49
120	2.09	10.96	0.45
130	2.05	10.32	1.28
140	2.01	10.04	1.98
150	1.96	9.98	2.55
160	1.9	10.06	2.96
170	1.84	10.21	3.23
180	1.78	10.38	3.34
190	1.73	10.52	3.3
200	1.67	10.62	3.14
210	1.61	10.68	2.87
220	1.57	10.7	2.51
230	1.52	10.7	2.08
240	1.49	10.69	1.6
250	1.46	10.67	1.08
260	1.45	10.67	0.54
270	1.44	10.69	-0.01

Table 4.2: Coaster range results for ϕ_o ranging from 90° to 270° . Range is maximized at $\phi_o=100$

We see that maximum dispersal range occurs at $\phi_o = 100$. Interestingly, this range maximizing position has neither the longest flight time nor the largest nor smallest z displacement. Near this range maximizing position, slight perturbations in ϕ_o correspond to large changes in both range and z displacement. This lack of robustness to perturbation in ϕ_o highlights the difficulty of actually achieving the range attained by this theoretically optimal orientation. Additionally the ϕ_o at which the peak occurs

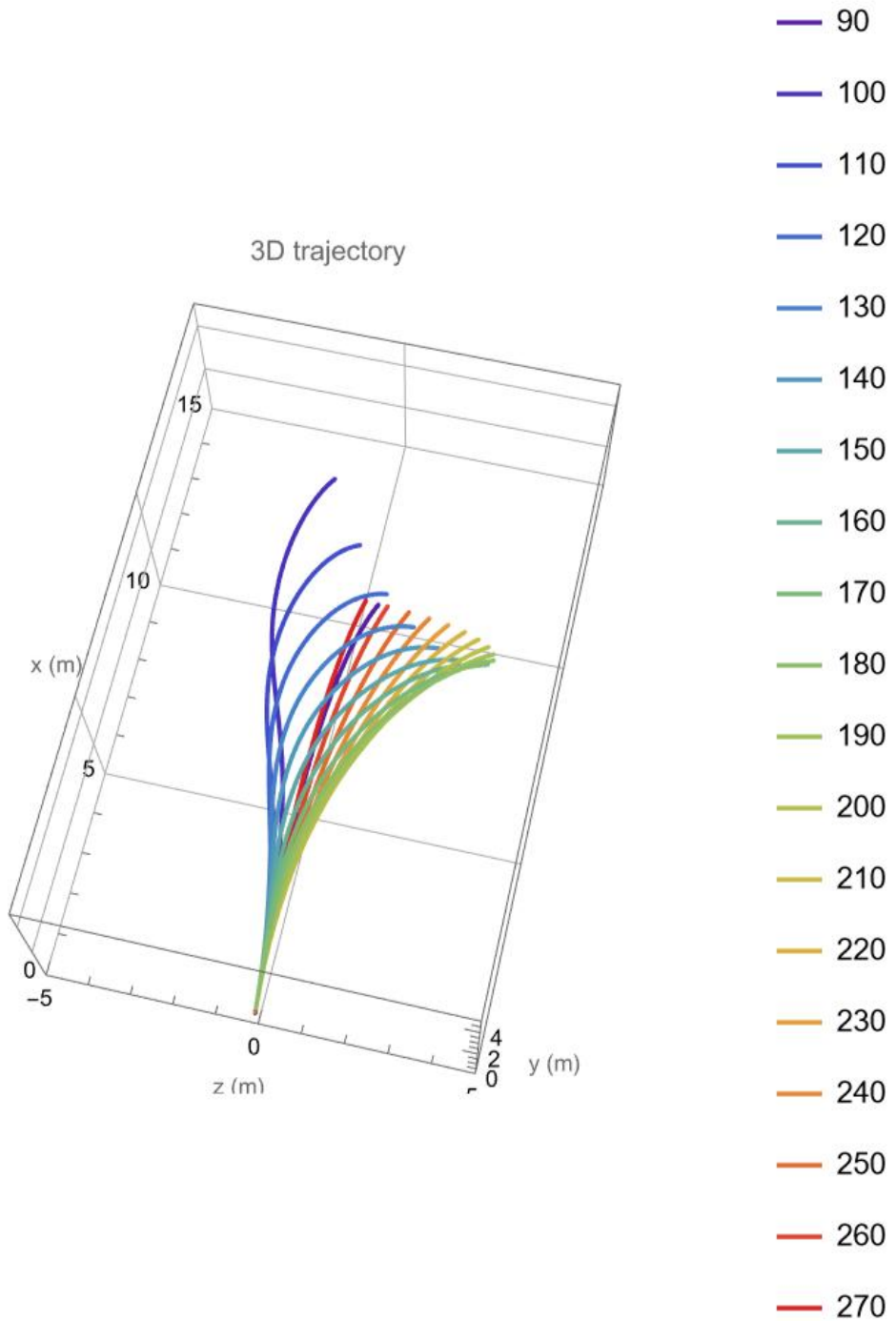


Figure 4.25: Three-dimensional trajectories of coasters under a range of ϕ_o from 90° to 270° . Orientations near topspin, but not exactly at topspin, are the range-maximizing orientation.

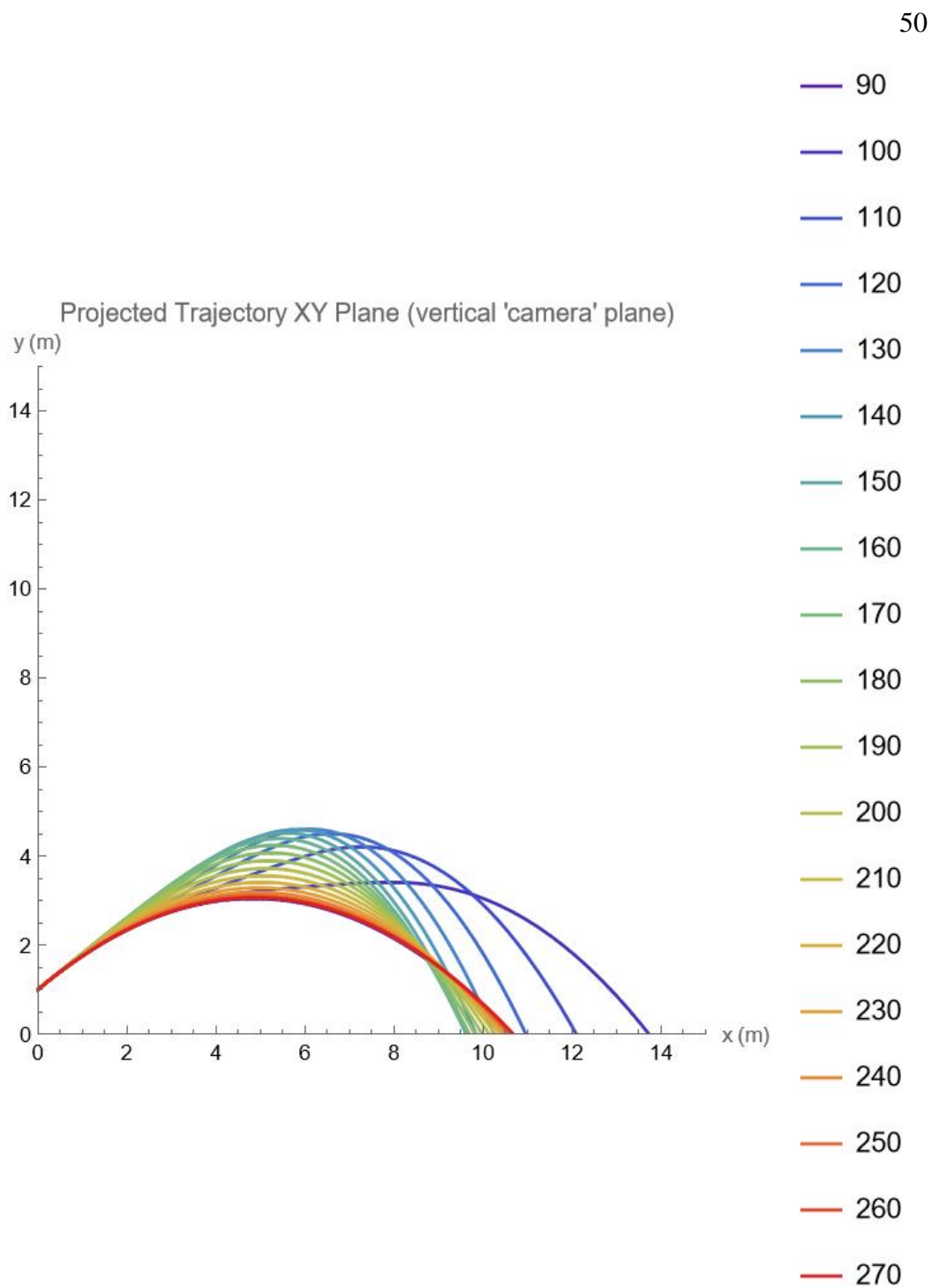


Figure 4.26: Range in the direction of initial velocity is shown to be maximized by the coaster launched near topspin.

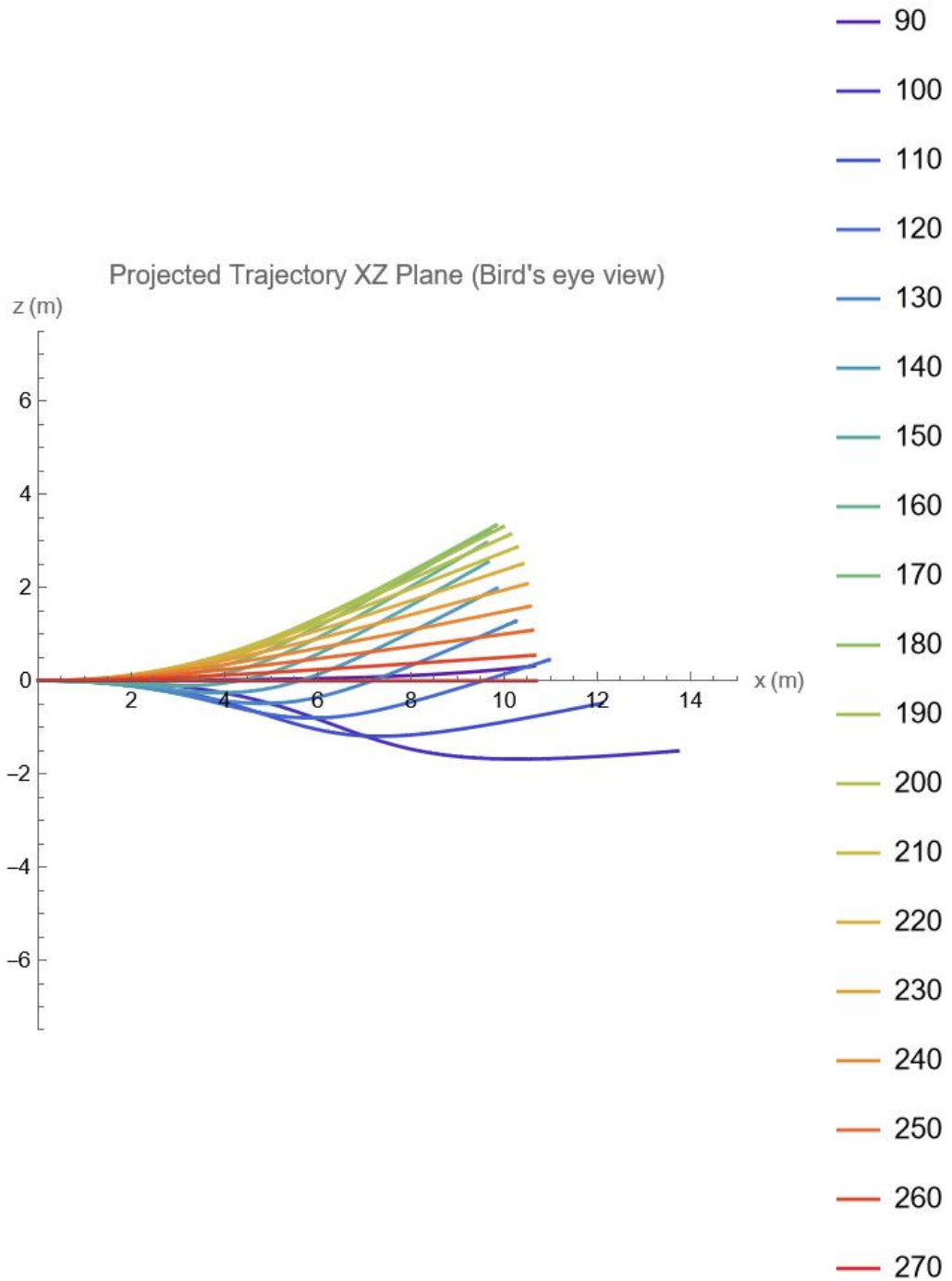


Figure 4.27: Vertical view of coaster trajectories shows near-topspin is the range maximizing orientation for the coaster launched with $\beta_o = 40^\circ$.

4.2 Seed Flight Simulations

Table 4.3 below gives the numeric values and 5% uncertainty intervals of the parameters used in this exploratory analysis.

Parameter	Description	Mean	St. Dev	N	5% Uncertainty
ϕ_o	Launch orientation	270°	-	-	-
β_o	Launch angle	40°	10°	79	±2
ω	Spin rate	1040 Hz	470 Hz	21	±220
$ \mathbf{V} $	Launch velocity	10 ms ⁻¹	3 ms ⁻³	79	±.7
m	Mass of disc	1.7 mg	.2 mg	9	±.2
r	Radius of disc	1.25 mm	.1 mm	10	±.07
d	Thickness of disc	.46 mm	.06 mm	7	±.05
C_M	Magnus Coefficient	0.035	0.07	44	±.02
C_D	Drag Coefficient	0.301	0.17	44	±.05
e	Induced drag efficiency	0.5	-	-	-

Table 4.3: *Ruellia ciliatiflora* seed launch parameters and morphology data, with 5% uncertainty intervals where applicable. Uncertainty calculated via $U = \pm \frac{\sigma t^*}{\sqrt{N}}$, where σ is standard deviation, t^* is the 95% Student t value, and N is the number of measurements. Data courtesy of Eric Cooper.

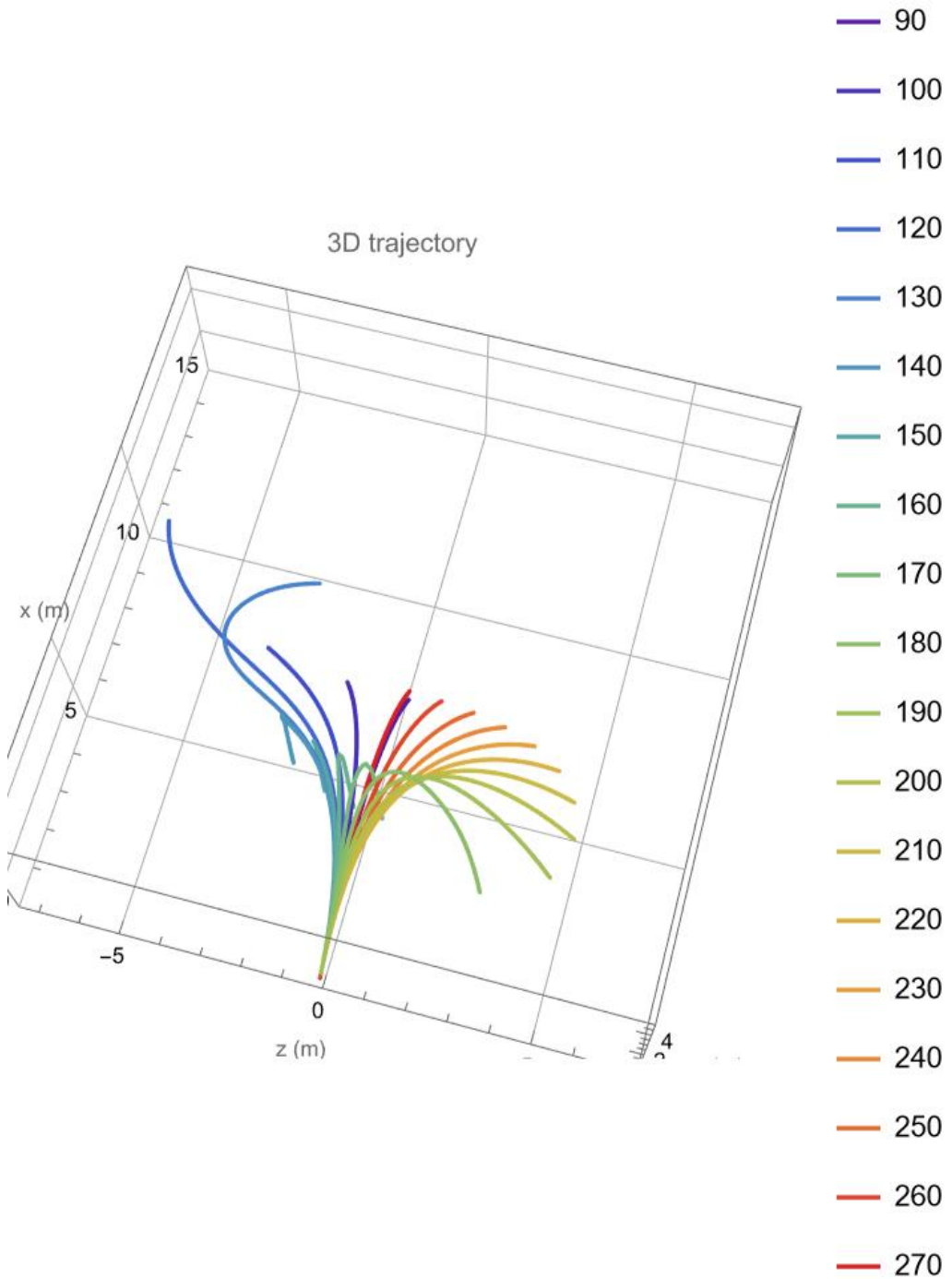


Figure 4.28: Three-dimensional trajectories of seeds under a range of ϕ_o from 90° to 270° . Orientations around $\phi_o = 110^\circ$ maximize dispersal range, but small changes to the initial orientation result in significant changes to the observed trajectory of the seed.

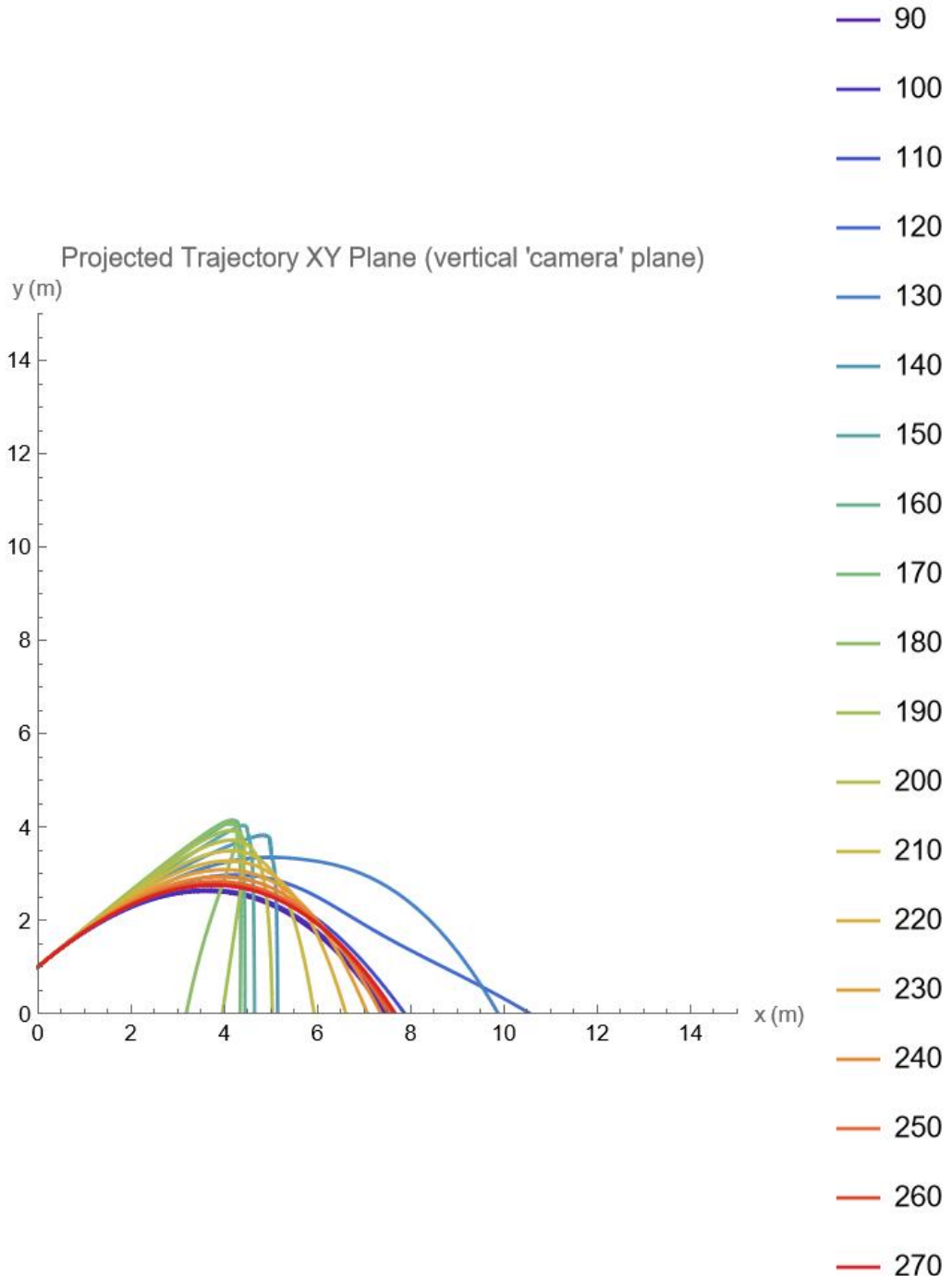


Figure 4.29: Range in the direction of initial velocity is shown to be maximized around 110° . Note that many initial orientations perform significantly worse than the backspin case in x displacement.

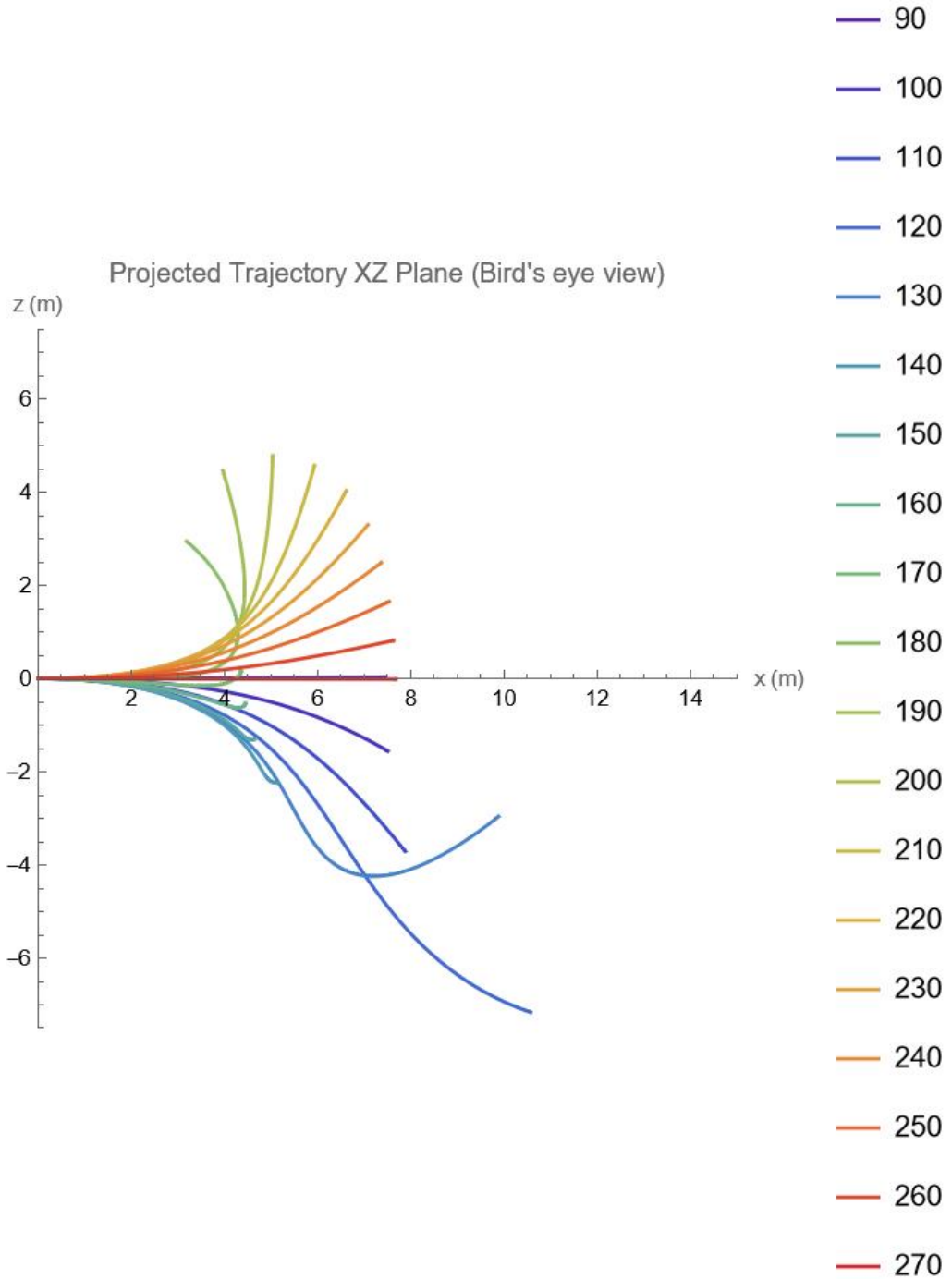


Figure 4.30: Vertical view of seed trajectories shows near-topspin is the range maximizing orientation, but small perturbations to initial orientation significantly impact observed trajectory and net displacement range. Many other launch orientations have significant z displacement, which can reduce their overall attained range.

In Figures 4.28 through 4.30, the simulated trajectories of *R. ciliatiflora* seeds are depicted. It is clear that certain initial orientations near $\phi_o = 110$ are capable of attaining impressive ranges greater than 12m. Compare this to backspin at $\phi_o = 270^\circ$, which only reaches about 7.5m. Note that, near topspin, slight changes in ϕ_o result in significant changes in the seed's trajectory and overall range attained. Compare this to backspin, where slight changes in initial launch orientation do not appreciably impact the trajectory nor range attained.

We can extend these simulations to a larger portion of parameter space. Table 4.4 below shows the range of parameters simulated.

Parameter	Description	Low Bound	Upper Bound	Step Size	Total
ϕ_o	Launch Orientation	90°	270°	2.5	73
β_o	Launch Angle	0°	64°	2	33
ω	Spin Rate	200 Hz	4000 Hz	200	39
h	Launch Height	0.5 m	1.0 m	.25	3
Total	—	—	—	—	281,853

Table 4.4: Range of parameters simulated. Total number of simulations: 281,853. Approximate 2hr runtime on my laptop, no parallelization. Yields roughly 2,500 simulations per minute.

The following three figures (4.31 through 4.33) are contours of horizontal dispersal distance over a range of initial ϕ_o and β_o . The grid lines are the ranges of these initial values that are regularly observed in actual *R. ciliatiflora* plants. The three contours vary only in their spin rates. Figure 4.31 uses $\omega = 500$ Hz, Figure 4.32 uses $\omega = 1000$ Hz, and Figure 4.33 uses $\omega = 1500$ Hz.

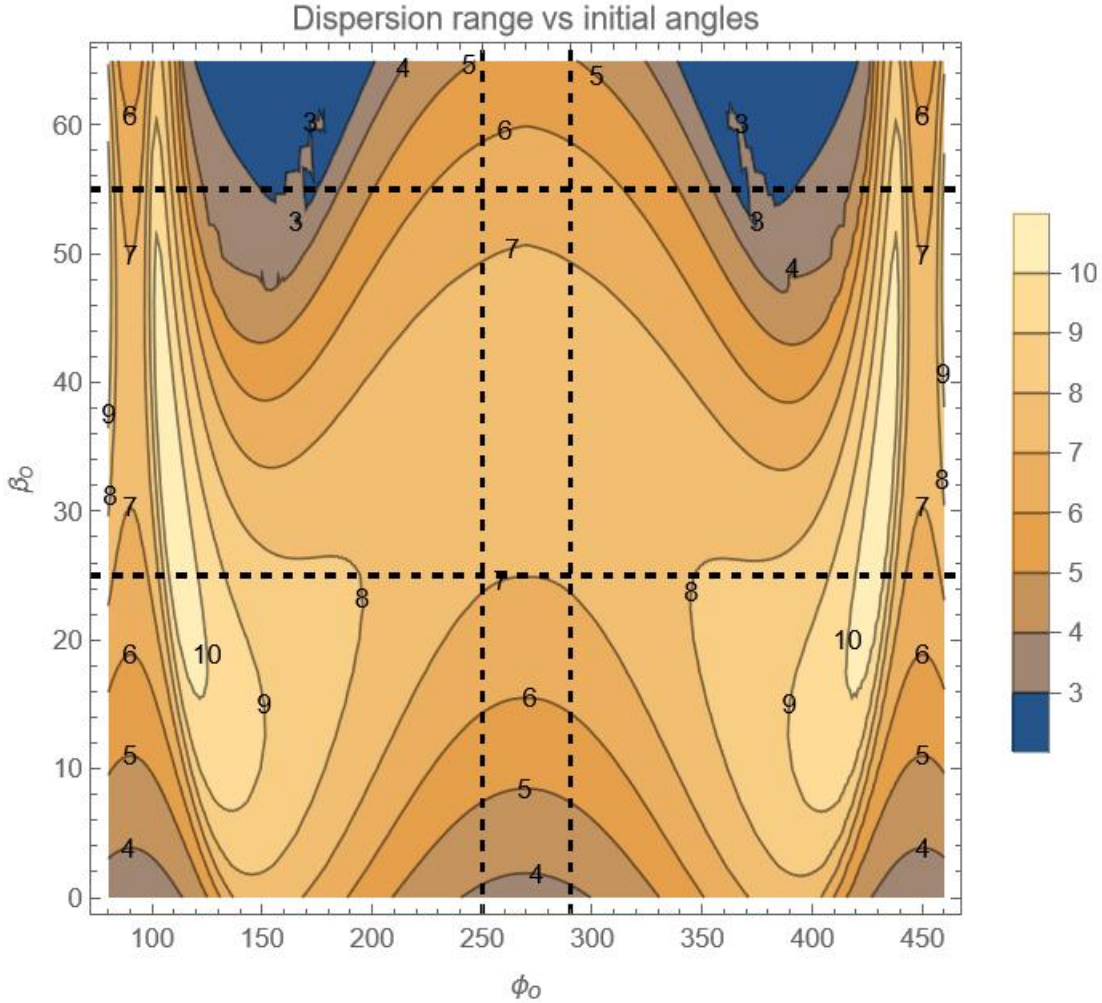


Figure 4.31: Range in the direction of initial velocity is shown to be maximized around 100° , with some slight dependence on β_o . This is a narrow peak, with slight perturbations in ϕ_o impacting the achieved range significantly. Compare this to backspin at $\phi_o = 270^\circ$. Moderate changes in ϕ_o and β_o do not significantly impact seed dispersal range.

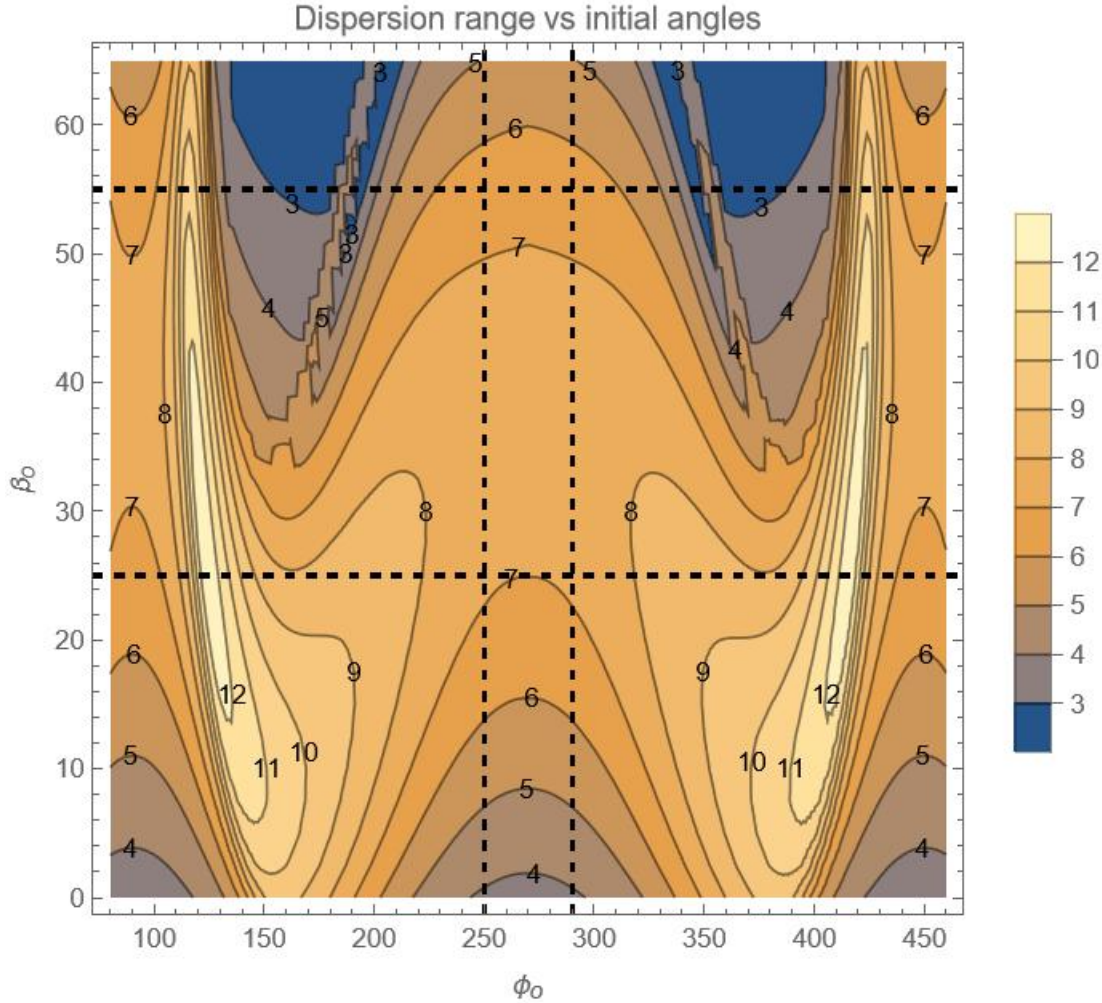


Figure 4.32: $\omega = 1000$ Hz. Range in the direction of initial velocity is shown to be maximized around 115° , with some slight dependence on β_o . The peak near $\phi_o = 115^\circ$ has narrowed compared to the $\omega = 500$ Hz case. The backspin plateau is largely unaffected by the changing ω .

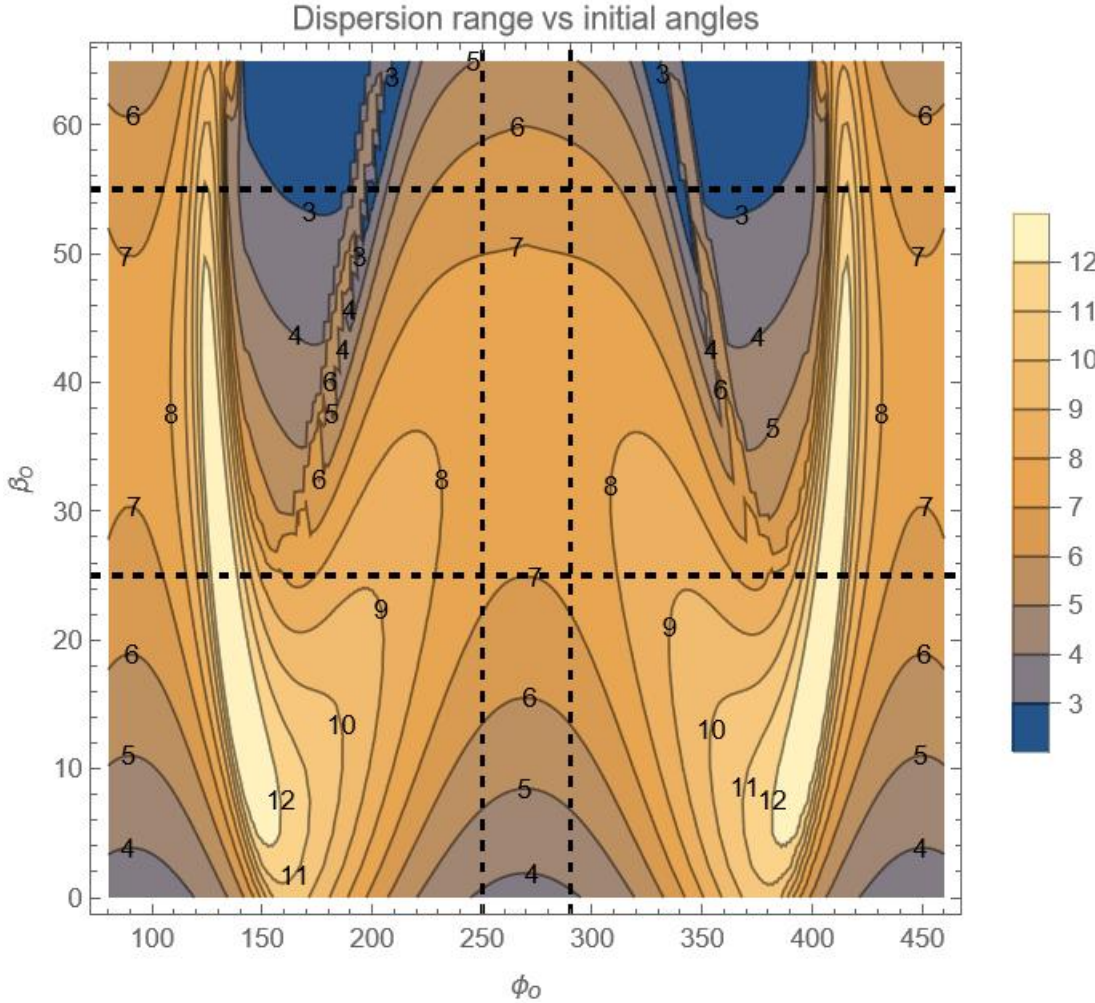


Figure 4.33: $\omega = 1500$ Hz. Range in the direction of initial velocity is shown to be maximized around 130° . This optimal peak has narrowed even further with the higher spin rate, making it even more difficult to achieve these larger dispersal ranges, and increasing risk of falling into the valley of failure.

As was seen in Figures 4.28 through 4.30, range is maximized slightly off of topspin, at ϕ_o s of about $100^\circ - 130^\circ$. However, this maximum peak is akin to a narrow ridge abutting a deep valley; slight perturbations in ϕ_o could easily displace the seed into this valley of failed launches. In contrast, backspin corresponds to a wide plateau at about 7m dispersal range. This plateau is robust to perturbations in β_o up to about $\pm 15^\circ$ and perturbations in ϕ_o on the order of about $\pm 40^\circ$ - launches occurring within this window do not suffer from seriously degraded launch performance.

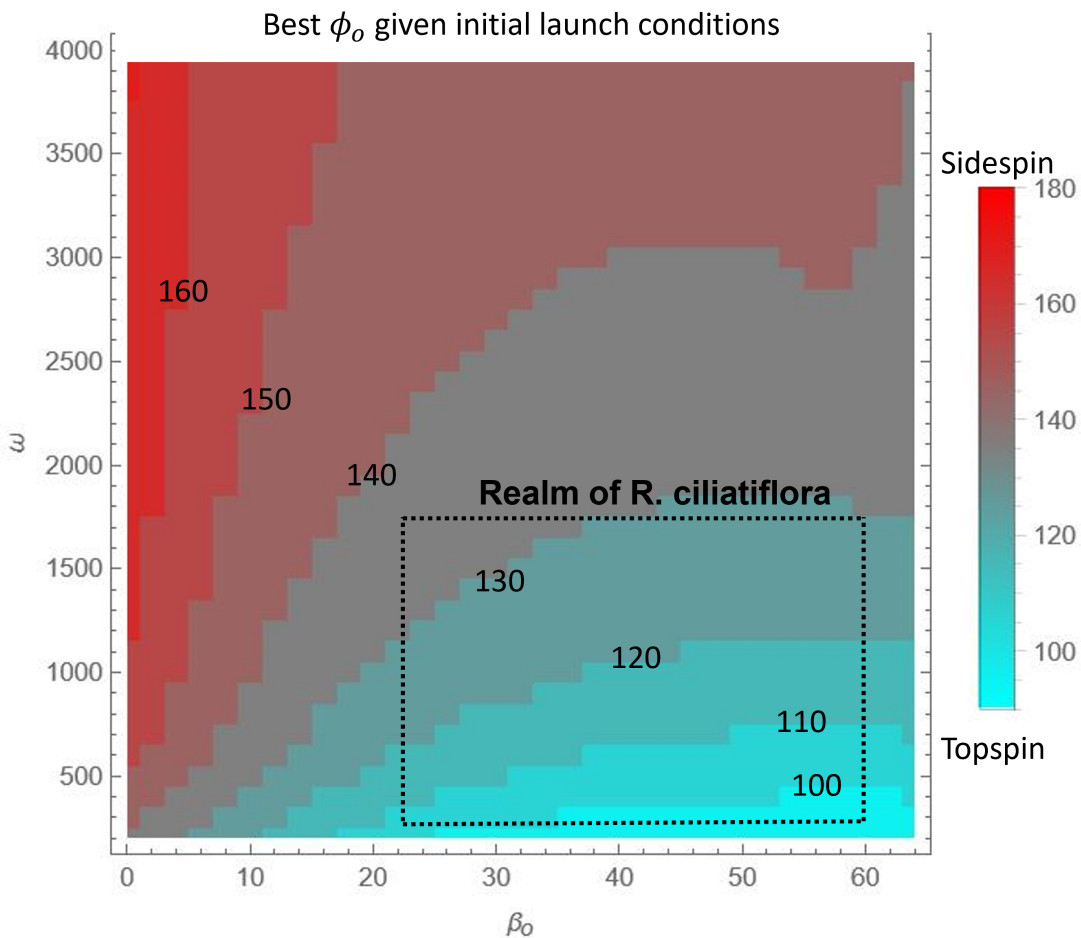


Figure 4.34: Contour showing the ϕ_0 that maximizes dispersal range for a given pair of β_0 and ω . Height is fixed at 0.75m. The boxed area shows the ranges of β_0 and ω that are frequently observed for *R. ciliatiflora* seeds. Within this range, the optimal ϕ_0 varies up to 40° . Recall from Figures 4.31 through 4.33 that perturbations greater than 20° can drop the dispersal range from the 12m ridge to the 3m valley.

Chapter 5

CONCLUSIONS AND FUTURE WORK

The seed trajectories for various ϕ_o s shown in Figures 4.28 through 4.30 demonstrate the susceptibility of the near-topspin orientation of *R. ciliatiflora* seeds to small perturbations in initial launch conditions. This precariousness is further emphasized in the contour plots shown in Figures 4.31 through 4.33. From these plots it is clear that the range maximizing launch orientation is a narrow peak that is difficult to consistently achieve. Furthermore, the proximity of the maximum range peak to the deep valley makes it risky to attempting to obtain this range maximizing launch orientation - missing the optimal ϕ_o by more than about $20^\circ - 30^\circ$ results in a failed launch that attains only 3m dispersal range. Meanwhile, Figure 4.34 shows that, for the ranges of launch angles and spin rates observed in dehiscence events of single fruits *R. ciliatiflora*, the optimal launch orientation ϕ_o varies up to 40° . As such, attempting to launch at the ideal launch orientation would almost certainly result in some of the seeds being launched at the orientations where range is significantly reduced.

In contrast, the contour plots of Figures 4.31 through 4.33 show that backspin is a much more robust launch orientation. Unlike the near-topspin orientations, the success of backspin does not depend on minor changes in launch angle, spin rate, launch height, or other launch or seed morphology characteristics. Launching near backspin ensures that, regardless of variability of initial launch parameters observed in seeds of a single fruit and across different fruits of *R. ciliatiflora*, all seed launches will be successful, assuming no defects exist in the fruit or seeds. Assuming that any launch orientation *could* have evolved, the fact that essentially all ballochores with disc-like seeds are observed to launch with backspin suggests that the ability to reliably achieve moderate launch ranges is more advantageous than the ability to launch seeds appreciably farther at the cost of reliability.

Future study into this topic could explore a variety of different avenues. For example, the numerical methods used in this thesis are generally robust, but there is likely some benefit to further analysis of the specifics of how solutions to the equation of motion are being generated. The code relies on the Mathematica black-box function `NDSolve` that largely obscure the details of how numerical solutions

to the equation of motion are obtained. The coaster data is generally smooth and well-behaved, but some of the extreme cases of seed simulations may be suspect. It seems there are possible numerical integration issues at some extreme values of initial launch orientations - updating the code to ensure Mathematica is using acceptable numerical methods would improve confidence in the results generated.

The existing codes are not optimized. There would be a benefit to optimizing the code to improve computing efficiency so that the number of simulations can be increased. Additionally, implementing parallel processing would significantly speed up computation time, as would transferring the code to high-performance computing resources available at the College.

For the existing codes created for this thesis, the magnitudes of several of the relevant parameters do not have a very sturdy theoretical or experimental basis. For example, the all that is known about the induced drag efficiency factor e is that it must lie between 0 and 1. The intermediate value of 0.5 was chosen arbitrarily. The evidence supporting the choice of Magnus coefficient is also not as exhaustive as it could be. The behavior of the Magnus coefficient with varied flow and seed morphology characteristics is not well understood. There even exists a flow regime where the Magnus coefficient becomes negative, acting in the opposite direction that would normally be expected. Experimental analysis of low aspect ratio cylinders of a variety of surface roughnesses is necessary to more carefully describe the Magnus effect.

This thesis examined only the effects of launch parameters on seed dispersal optimality; further study into *R. ciliatiflora* seed dispersal could examine the effect of varied seed morphologies on launch effectiveness. Since the trajectory of the backspin orientation is essentially equivalent to that of a simple particle experiencing quadratic drag, varied seed morphology seems unlikely to impact backspin trajectories significantly. In contrast, since the optimal near-topspin orientation is attained through a precise tuning of various launch parameters, it seems more likely that perturbations in seed morphologies have the potential to significantly impact flight trajectories, again suggesting an advantage in the simplicity of the backspin launch mechanism.

Finally, after *R. ciliatiflora* is fully studied, expanding the work to other ballochores with disc-like seeds could provide additional support for the robustness hypothesis or suggest other relevant factors not revealed by the analysis of *R. ciliatiflora*.

BIBLIOGRAPHY

- [1] John D. Anderson. *Fundamentals of aerodynamics*. en. Sixth edition. McGraw-Hill series in aeronautical and aerospace engineering. New York, NY: McGraw Hill Education, 2017. ISBN: 978-1-259-12991-9.
- [2] Carmine Badalamenti and Simon Prince. “Effects of Endplates on a Rotating Cylinder in Crossflow”. en. In: *26th AIAA Applied Aerodynamics Conference*. Honolulu, Hawaii: American Institute of Aeronautics and Astronautics, Aug. 2008. ISBN: 978-1-60086-987-7. DOI: 10.2514/6.2008-7063. URL: <https://arc.aiaa.org/doi/10.2514/6.2008-7063>.
- [3] Brennen. *The Flat Plate Airfoil*. URL: <http://brennen.caltech.edu/fluidbook/externalflows/lift/flatplateairfoil.pdf>.
- [4] J. M. Bullock and R. T. Clarke. “Long distance seed dispersal by wind: measuring and modelling the tail of the curve”. en. In: *Oecologia* 124.4 (Sept. 2000), pp. 506–521. ISSN: 0029-8549. DOI: 10.1007/PL00008876. URL: <http://link.springer.com/10.1007/PL00008876>.
- [5] Si-Chong Chen et al. “Trade-off or coordination? Correlations between ballochorous and myrmecochorous phases of diplochory”. en. In: *Functional Ecology* 33.8 (Aug. 2019). Ed. by Daniel García, pp. 1469–1479. ISSN: 0269-8463, 1365-2435. DOI: 10.1111/1365-2435.13353. URL: <https://onlinelibrary.wiley.com/doi/10.1111/1365-2435.13353>.
- [6] Eric Cooper and Dwight Whitaker. “The Aerodynamics of Seed Dispersal in Acanthaceae”. en. PhD thesis. Pomona College, May 2018.
- [7] Eric S. Cooper et al. “Gyroscopic stabilization minimizes drag on *Ruellia ciliatiflora* seeds”. en. In: *Journal of The Royal Society Interface* 15.140 (Mar. 2018), p. 20170901. ISSN: 1742-5689, 1742-5662. DOI: 10.1098/rsif.2017.0901. URL: <https://royalsocietypublishing.org/doi/10.1098/rsif.2017.0901>.
- [8] Cathal Cummins et al. “A separated vortex ring underlies the flight of the dandelion”. en. In: *Nature* 562.7727 (Oct. 2018), pp. 414–418. ISSN: 0028-0836, 1476-4687. DOI: 10.1038/s41586-018-0604-2. URL: <http://www.nature.com/articles/s41586-018-0604-2>.
- [9] H F Howe and J Smallwood. “Ecology of Seed Dispersal”. en. In: *Annual Review of Ecology and Systematics* 13.1 (Nov. 1982), pp. 201–228. ISSN: 0066-4162. DOI: 10.1146/annurev.es.13.110182.001221. URL: <http://www.annualreviews.org/doi/10.1146/annurev.es.13.110182.001221>.
- [10] Jade Hyslop and Sam Trowsdale. “A review of hydrochory (seed dispersal by water) with implications for riparian rehabilitation”. en. In: (2021), p. 17.

- [11] *Induced drag coefficient*. URL: <https://www.grc.nasa.gov/www/k-12/airplane/induced.html>.
- [12] *Introduction to advanced numerical differential equation solving*. URL: <https://reference.wolfram.com/language/tutorial/NDSolveIntroductoryTutorial.html>.
- [13] *Introduction to Numerical Differential Equations*. URL: <https://reference.wolfram.com/language/tutorial/NumericalOperationsOnFunctions.html#8415>.
- [14] T.T. Kozlowski. *Seed Biology: Importance, Development, and Germination*. Elsevier, 1972.
- [15] L. A. McDade, T. F. Daniel, and C. A. Kiel. “Toward a comprehensive understanding of phylogenetic relationships among lineages of Acanthaceae S.L. (Lamiales)”. In: *American Journal of Botany* 95.9 (2008), pp. 1136–1152. doi: [10.3732/ajb.0800096](https://doi.org/10.3732/ajb.0800096).
- [16] Johann Ostmeyer, Christoph Schürmann, and Carsten Urbach. “Beer mats make bad frisbees”. en. In: *The European Physical Journal Plus* 136.7 (July 2021), p. 769. ISSN: 2190-5444. doi: [10.1140/epjp/s13360-021-01732-1](https://doi.org/10.1140/epjp/s13360-021-01732-1). URL: <https://link.springer.com/10.1140/epjp/s13360-021-01732-1>.
- [17] Simon Poppinga et al. “A seed flying like a bullet: ballistic seed dispersal in Chinese witch-hazel (*Hamamelis mollis* OLIV., Hamamelidaceae)”. en. In: *Journal of The Royal Society Interface* 16.157 (Aug. 2019), p. 20190327. ISSN: 1742-5689, 1742-5662. doi: [10.1098/rsif.2019.0327](https://doi.org/10.1098/rsif.2019.0327). URL: <https://royalsocietypublishing.org/doi/10.1098/rsif.2019.0327>.
- [18] Abel I. Rouboa et al. “Analysis of wind velocity and release angle effects on discus throw using computational fluid dynamics”. In: *Computer Methods in Biomechanics and Biomedical Engineering* 16.1 (2013), pp. 73–80. doi: [10.1080/10255842.2011.607443](https://doi.org/10.1080/10255842.2011.607443).
- [19] *Shape effects on drag*. URL: <https://www.grc.nasa.gov/www/k-12/airplane/shaped.html>.
- [20] Erin A. Tripp and Lucinda A. McDade. “A rich fossil record yields calibrated phylogeny for Acanthaceae (Lamiales) and evidence for marked biases in timing and directionality of intercontinental disjunctions”. In: *Systematic Biology* 63.5 (2014), pp. 660–684. doi: [10.1093/sysbio/syu029](https://doi.org/10.1093/sysbio/syu029).
- [21] Xander M. Van Der Burgt. “Explosive seed dispersal of the rainforest tree *Tetraberlinia moreliana* (Leguminosae – Caesalpinioideae) in Gabon”. en. In: *Journal of Tropical Ecology* 13.1 (Jan. 1997), pp. 145–151. ISSN: 0266-4674, 1469-7831. doi: [10.1017/S0266467400010336](https://doi.org/10.1017/S0266467400010336). URL: https://www.cambridge.org/core/product/identifier/S0266467400010336/type/journal_article.

- [22] Pascal Vittoz and Robin Engler. “Seed dispersal distances: a typology based on dispersal modes and plant traits”. en. In: *Botanica Helvetica* 117.2 (Dec. 2007), pp. 109–124. ISSN: 0253-1453, 1420-9063. DOI: 10.1007/s00035-007-0797-8. URL: <http://link.springer.com/10.1007/s00035-007-0797-8>.
- [23] Steven Vogel. “The Flight of the Seed of *Hura crepitans*”. en. In: (), p. 5.
- [24] Dwight L. Whitaker and Joan Edwards. “Sphagnum moss disperses spores with vortex rings”. In: *Science* 329.5990 (2010), pp. 406–406. DOI: 10.1126/science.1190179.
- [25] A. Witztum and K. Schulgasser. “The mechanics of seed expulsion in Acanthaceae”. In: *Journal of Theoretical Biology* 176.4 (1995), pp. 531–542. DOI: 10.1006/jtbi.1995.0219.